Compare Results

Old File:		New File:
KRK_preprint-2.pdf	versus	**KRK_review1_20210630.pdf**
31 pages (15.82 MB)		**32 pages (18.08 MB)**
22/04/2021, 12:21:38		30/06/2021, 17:06:16

Total Changes

431

Text only comparison

Content

177 Replacements

140 Insertions

114 Deletions

Styling and Annotations

0 Styling

0 Annotations

Go to First Change (page 1)

Methane (CH_4) sources in Krakow, Poland: insights from isotope analysis

Malika Menoud[1], Carina van der Veen[1], Jaroslaw Necki[2], Jakub Bartyzel[2], Barbara Szénási[3], Mila Stanisavljević[2], Isabelle Pison[3], Philippe Bousquet[3], and Thomas Röckmann[1]

[1]Institute for Marine and Atmospheric research Utrecht (IMAU), Utrecht University, Utrecht, The Netherlands
[2]Faculty of Physics and Applied Computer Science, AGH University of Science and Technology, Kraków, Poland
[3]Laboratoire des sciences du climat et de l'environnement (LSCE), Université Paris-Saclay, CEA, CNRS, UVSQ, Gif-sur-Yvette, France

Correspondence: Malika Menoud (m.menoud@uu.nl)

Abstract. Methane (CH_4) emissions from human activities are a threat to the resilience of our current climate system. The stable isotopic composition of methane ($\delta^{13}C$ and δ^2H) allows to distinguish between the different CH_4 origins. A significant part of the European CH_4 emissions, 3.6 % in 2018, comes from coal extraction in Poland; the Upper Silesian Coal Basin (USCB) being the main hotspot.

5   Measurements of CH_4 mole fraction ($\chi(CH_4)$), $\delta^{13}C$ and δ^2H in CH_4 in ambient air were performed continuously during 6 months in 2018 and 2019 at Krakow, Poland, in the east of the USCB. In addition, air samples were collected during parallel mobile campaigns, from multiple CH_4 sources in the footprint area of the continuous measurements. The resulting isotopic signatures from sampled plumes allowed us to distinguish between natural gas leaks, coal mine fugitive emissions, landfill and sewage, and ruminants. The use of δ^2H in CH_4 is crucial to distinguish the fossil fuel emissions in the case of

10   Krakow, because their relatively depleted $\delta^{13}C$ values overlap with the ones of microbial sources. The observed $\chi(CH_4)$ time series showed regular daily night-time accumulations, sometimes combined with irregular pollution events during the day. The isotopic signatures of each peak were obtained using the Keeling plot method, and generally fall in the range of thermogenic CH_4 formation - with $\delta^{13}C$ between -59.3 and -37.4 ‰ V-PDB, and δ^2H between -291 and -137 ‰ V-SMOW. They compare well with the signatures measured for gas leaks in Krakow and USCB mines.

15   The CHIMERE transport model was used to compute the CH_4 and isotopic composition time series in Krakow, based on two emission inventories. The magnitude of the pollution events is generally under-estimated in the model, which suggests that emission rates in the inventories are too low. The simulated isotopic source signatures, obtained with Keeling plots on each simulated peak, indicate that a higher contribution from fuel combustion sources in the EDGAR v5.0 inventory would lead to a better agreement than when using CAMS-REG-GHG v4.2. The isotopic mismatches between model and observations are

20   mainly caused by uncertainties in the assigned isotopic signatures for each source category, and the way they are classified in the inventory. These uncertainties are larger for emissions close to the study site, which are more heterogenous than the ones advected from the USCB coal mines. Our isotope approach proves to be very sensitive in this region, thus helping to evaluate emission estimates.

1 Introduction

25 Atmospheric emissions of greenhouse gasses, defined as gas compounds that absorb and emit thermal infrared radiations, from human activities are the main cause of the current warming of our Earth's climate. It is urgent to decrease these emissions in order to minimise the negative consequences of climate change on people and societies (IPCC (2018)). The second most important greenhouse gas of anthropogenic origin after carbon dioxide (CO_2) is methane (CH_4; IPCC (2018)). CH_4 has a Global Warming Potential (GWP; integrated radiative forcing relative to that of CO_2 per kg of emission) of 86 over a 20 year

30 time horizon, including carbon cycle feedbacks (IPCC (2013)). On a global scale, 23 % of the additional radiative forcing since 1750 is attributed to CH_4, whereas total CH_4 anthropogenic emissions represent only 3 % those of CO_2 in term of carbon mass flux (Etminan et al. (2016)). In recent years, total CH_4 emissions have been rising: they increased by 5 % in the period 2008-2017 (and 9 % in 2017), compared to the period 2000-2006 (Saunois et al. (2020)). It is not clear which sources have caused these changes, but Saunois et al. (2020) estimated anthropogenic emissions to represent 60 % of the total emissions

35 of the past 10 years. Nisbet et al. (2019) showed that the current levels of CH_4 emissions are a threat to the adherence of the Paris Agreement goals, but an effective reduction of CH_4 emissions requires knowledge of the locations and magnitudes of the different sources.

Atmospheric measurements of greenhouse gasses at several locations have been used to investigate the rates, origins, and variations in emissions. However, for methane, these are not always in agreement with what is reported in the emissions

40 inventories (Saunois et al. (2020)). Isotopic measurements are used to better constrain the sources of methane at regional (e.g. Levin et al. (1993), Tarasova et al. (2006), Beck et al. (2012), Röckmann et al. (2016), Townsend-Small et al. (2016), Hoheisel et al. (2019), Menoud et al. (2020b)) and global scales (e.g. Monteil et al. (2011), Rigby et al. (2012), Schwietzke et al. (2016), Schaefer et al. (2016), Nisbet et al. (2016), Worden et al. (2017), Turner et al. (2019)). Indeed, the different CH_4 generation pathways lead to different isotopic signatures (Milkov and Etiope (2018), Sherwood et al. (2017), Quay et al.

45 (1999)). Recently, instruments for continuous measurements of the isotopic composition of CH_4 have been developed (Eyer et al. (2016), Chen et al. (2016), Röckmann et al. (2016)) and used to characterise the main sources of a specific region (Röckmann et al. (2016), Yacovitch et al. (2020), Menoud et al. (2020b)). Using model simulations, the observations can be used to evaluate the partitioning of the different sources reported in the inventories (Rigby et al. (2012), Szénási (2020)).

Saunois et al. (2020) stated the need for more measurements in regions where very few observations are available so far. In

50 Europe, inventories report high CH_4 emissions from Poland (European Environment Agency (2019)). In 2018, they represented 10 % of total European Union emissions, with more than 48 Mt CO_2 eq.. Half of these are from the energy sector, among which 72 % are due to the exploitation of underground coal mines (National Centre for Emission Management (KOBiZe) and Institute of Environmental Protection - National Research Institute (2020), Swolkień (2020)). The Upper Silesian Coal Basin (USCB), where most mining activity occurs in Poland, is certainly a CH_4 emission hotspot in Europe. Atmospheric measurements at

55 the USCB were mostly performed in the recent years (Swolkień (2020), Luther et al. (2019), Gałkowski et al. (2020), Fiehn et al. (2020)), and focused on the coal extraction activities. The CH_4 emission rates were estimated at the regional scale (Luther et al. (2019), Fiehn et al. (2020)), with a relatively good agreement with the inventories (Luther et al. (2019), Fiehn

et al. (2020), Gałkowski et al. (2020)). Swolkień (2020) performed direct measurements of CH_4 fluxes at individual shafts and emphasised the large variability of emission pattern between different sites. A general isotopic signature from USCB CH_4 sources was recently determined by Gałkowski et al. (2020), with values of -50.9 $\pm$ 1.1 ‰ for $\delta^{13}C$ and -224.7 $\pm$ 6.6 ‰ for δ^2H. These values, based on aircraft measurements, compare well with previous measurements at individual shafts for $\delta^{13}C$, but are significantly lower for δ^2H. The area covered by the USCB includes other sources of methane, such as ruminant farming and waste degradation. In this study we investigate whether we can use isotopic signals to distinguish the different sources from a densely populated area like Krakow. We wanted to establish the main CH_4 sources affecting the city. Finally, we investigate whether we can use this tool to put constrains on the emission inventories in order to improve them.

To this end, we carried out and investigated quasi-continuous measurement of CH_4 mole fraction, $^{13}C/^{12}C$ and $^2H/^1H$ isotopic ratios of CH_4 in ambient air during 6 months at a fixed location in Krakow, Poland. Time series of these isotopic ratios were also simulated with an atmospheric transport model, based on two different emission inventories. The local CH_4 sources were sampled during several mobile measurement campaigns, to determine their isotopic signatures and compare with the ambient measurements.

2 Methods

2.1 Target region and time period

The region of study is characterised by the presence of a large coal mining region: the Upper Silesian Coal Basin (USCB). It has 20 active coal mines spread over an area of 1100 km^2 (Swolkień (2020)), and the closest shafts are located about 40 km west of Krakow (Fig. 1). Other potential CH_4 sources around Krakow are from waste management and wastewater treatment facilities, industrial activity, energy production and the natural gas distribution network. Large-scale agriculture activities are not characteristic for this area, and only very few cattle farms could be located.

Ambient air measurements were performed from the Faculty of Physics and Applied Computer Science building, at AGH university in Krakow (50°04'01.1"N, 19°54'46.9"E, Fig. 1). We used a 1/2" o.d. Synflex Dekabon air intake line that draws air from the top of a mast on top of the building (35 m above ground level, 255 m a.s.l.) down to the laboratory of the Environmental Physics Group. A fraction of the incoming air was directed via a T-split to the IRMS system in the period from September 14th, 2018 to March 14th, 2019. To place the CH_4 enhancements in perspective, the data was compared with measurements of background CH_4 made by the KASLAB (high-altitude laboratory of greenhouse gas measurement) at the top of at Kasprowy Wierch, a mountain in southern Poland (49°13'57"N, 19°58'55"E, 1989 m a.s.l.; Necki et al. (2013)).

Individual emission locations of methane were visited in and around the city of Krakow, and in the USCB during mobile surveys. The surveys were performed in May 2018 (from 24th to 29th), February 2019 (from 5th to 7th) and March 2019 (from 20th to 22nd). We visited the following areas, which are shown on the map in Fig. 1: the Silesian coal basin, Barycz landfill, the industrial park, the city center and other residential areas, and rural areas west of the city.

2.2 Sampling

The mobile surveys were conducted with an Integrated Cavity Output Spectroscopy (ICOS) instrument (MGGA - 918, Microportable Greenhouse Gas Analyser, Los Gatos Research, ABB) onboard of a car. An 1/8" Parflex inlet line was placed on top of the vehicle's roof and connected to the analyser. Real time CH_4 mole fractions were read on a tablet screen, so that an emission plume could be detected while driving. If the increase was higher than 200 ppb above background, we drove back to the plume and took one to three samples directly from the outflow of the CH_4 analyser, using sampling bags (Supel™-Inert Multi-Layer Foil, Sigma-Aldrich Co. LLC).

One or two samples were taken where we observed the lowest $\chi(CH_4)$ during each survey day, in order to obtain the background we can associate with the plumes sampled each day in a certain area.

The samples collected during the mobile surveys were analysed on the same IRMS instrument as the ambient air, partly when it was installed in Krakow, and partly when it was installed back at the IMAU lab in Utrecht.

2.3 Isotopic measurements

The $^{13}C/^{12}C$ and $^2H/^1H$ isotope ratios in CH_4 are expressed as $\delta^{13}C$ and δ^2H (deuterium), respectively, in per mil (‰), relative to the international reference materials, Vienna Pee Dee Belmnite (V-PDB) for $\delta^{13}C$ and Vienna Standard Mean Ocean Water (V-SMOW) for δ^2H.

The isotopic composition measurements were performed using an Isotope Ratio Mass Spectrometry (IRMS) system, as described in Röckmann et al. (2016) and Menoud et al. (2020b). Ambient air or sample air measurements were interspersed with measurements of a reference cylinder filled with air with assigned composition of $\chi(CH_4)$ = 1950.3 ppb, $\delta^{13}C$-CH_4 = -47.82 $\pm$ 0.09 ‰ V-PDB, and δ^2H-CH_4 = -92.2 $\pm$ 1.8 ‰ V-SMOW. The reference air bottle was previously calibrated against a reference gas measured at the Max Planck Institute in Jena, Germany (Sperlich et al. (2016)).

The extraction and measurement steps are illustrated in Fig. S1 of the supplementary material. Each measurement of either $\delta^{13}C$ or δ^2H returned a value of CH_4 mole fraction ($\chi(CH_4)$), calculated from the area of the IRMS peak obtained for the sample, compared to the area of air from a reference gas cylinder filled with air with 1950.3 ppb CH_4. This cylinder was calibrated against a reference gas measured by the Max Planck Institute for Biogeochemistry, Jena, Germany. The reproducibility of our measurements is of 16 ppb for $\chi(CH_4)$, 0.07 ‰ for $\delta^{13}C$ and 1.7 ‰ for δ^2H. A $\delta^{13}C$-CH_4 or δ^2H-CH_4 value in ambient air was obtained on average every 27 minutes during the periods of normal operation. In addition to unexpected disturbances or failures, the scheduled replacement of several components (oven catalysts, chemical dryer, fittings, etc.) and the regular flushing and heating of the traps required to stop the measurements for a few hours up to a few days, several times during the study period.

The air was simultaneously measured by a CRDS instrument (G2201-i Isotopic Analyzer, Picarro) installed in the same lab as the IRMS system and drawing air from the same inlet tube. Time series of CH_4 mole fractions from both instruments were compared for quality control, but we did not evaluate the isotopic ratios from the CRDS. The instrument precision for the CH_4 mole fraction is of 6 ppb, as reported by the manufacturer.

2.4 Meteorological data

Data on the hourly wind direction, speed, and temperature were obtained from an automatic weather station (Vaisala WXT520, Vaisala inc.) installed on the same building as the inlet line (220 m a.s.l.). The station is operated by the Environmental Physics Group, and the data is publicly available at http://meteo.ftj.agh.edu.pl/archivalCharts (registration required). Data on PM10 concentrations is also available on the same platform at this location.

2.5 Modelling

Time series of $\delta^{13}C$ and δ^2H -CH$_4$ were generated from simulated CH$_4$ mole fractions using the CHIMERE atmospheric transport model (Menut et al. (2013), Mailler et al. (2017)), driven by the PYVAR system (Fortems-Cheiney et al. (2019)). CHIMERE is a three-dimensional Eulerian limited-area chemistry-transport model for the simulation of regional atmospheric concentrations of gas-phase and aerosol species.

The simulations were carried out at a horizontal resolution of 0.1 $^\circ$ x 0.1 $^\circ$ in a domain covering Poland and nearby countries; [46.0° - 55.9°] in latitude and [12.0° - 25.9°] in longitude. The meteorological data used to drive CHIMERE were obtained from the European Centre for Medium-Range Weather Forecast (ECMWF) operational forecast product. The boundary and initial concentrations of $\chi(CH_4)$ were taken from the analysis and forecasting system developed in the Monitoring Atmospheric Composition and Climate (MACC) project (Marécal, 2015). They were used to derive the background CH$_4$ mole fractions.

The CH$_4$ emission rates over the domain are reported in emission inventories, following a bottom-up approach. We used two anthropogenic emission inventories for this study: EDGAR v5.0 (Emission Database for Global Atmospheric Research, Crippa et al. (2019)) and CAMS-REG-GHG v4.2 (The Copernicus Atmosphere Monitoring Service REGional inventory for Air Pollutants and GreenHouse Gases, Granier et al. (2012)). We classified the emissions in 6 anthropogenic source categories based on the European Environment Agency (EEA) greenhouse gas inventory common reporting format (CRF, European Environment Agency (2019)). We considered one additional category for natural wetland emissions, which are obtained from the ORCHIDEE-WET process model (Ringeval et al. (2011)). The classifications used in CHIMERE and the corresponding categories in the inventories are summarised in Table 1.

The isotopic values at each time t were calculated using the following formula:

$$\delta_t = \frac{1}{c_t} \sum_i^{n_S} (c_{S,i} * \delta_{S,i})$$

with c_t the total mole fraction from the model at time t, c_S the modelled mole fraction attributed to the source S, and δ_S the source signature of each specific source S. In this mass balance, the contribution of the background is treated as a source with assigned isotopic composition. All the assigned source signatures are defined in Table 1.

2.6 Isotopic signatures assigned to CH$_4$ enhancements

Periods of methane enhancement were identified from the $\chi(CH_4)$ time series using a peak extraction method, based on the detection of local maxima from comparison with the neighbouring points. The peaks were selected based on two criteria:

- the peak has a minimal amplitude of 100 ppb

- the peak is composed of at least three data points, from the maximum to a relative height of 0.6 times the peak height.

155 In order to define the background more robustly, we included additional data from the 10th lower percentile of $\chi(CH_4)$ in a window of $\pm$ 24 h around the maximum of each peak. The Keeling plot method was thus applied to the data points in the peak, together with the neighbouring background data.

The Keeling plot is a mass balance approach (Keeling (1961), Pataki et al. (2003)), considering the measured CH_4 (m) in ambient air as the sum of a contribution of CH_4 from an emission source (s) and a background (bg) CH_4, such that:

160 $c_m = c_{bg} + c_s$

$c_m \delta_m = c_{bg} \delta_{bg} + c_s \delta_s$

with c and δ referring to the mole fraction and isotopic signatures of either ^{13}C or ^2H, respectively. Re-arranging the formula leads to:

165 $\delta_m = c_{bg} * (\delta_{bg} - \delta_s)(1/c_m) + \delta_s$

We assumed the background mole fraction and isotopic composition to be stable over the time period of each peak. In this case, δ_s is given by the y-intercept of the regression line, when plotting δ_m against $1/c_m$.

To derive an average source signature for the entire dataset, the Miller-Tans approach was used (Miller and Tans (2003)), because the hypothesis of stable background is violated. This method is based on the following formula:

170 $c_m \delta_m = \delta_s c_m - c_{bg}(\delta_{bg} - \delta_s)$

where δ_s is now given by the slope of the regression line, when plotting $c_m * \delta_m$ against c_m.

An isotopic signature was obtained from the linear regressions, and the corresponding uncertainty was derived as 1 standard deviation of the estimated parameter (intercept for the Keeling plot or slope for the Miller-Tans plot). For all Keeling plots, the weighted Orthogonal Distance Regression (ODR) fitting method (Boggs et al. (1992)) was used.

175 The method was applied to both $\delta^{13}C$ and δ^2H measurement results. If two peaks were detected within a 6 hour time window in the $\delta^{13}C$ and δ^2H time series, they were considered one single peak and the two signatures were allocated to it. The same method was also used for the modelled $\chi(CH_4)$ time series, to allow the comparison of modelled and measured source signatures.

The Keeling plot method was also used to calculate source isotopic signatures for each location where we sampled CH_4

180 enhancements during the mobile surveys. The determined source signatures were accepted if they fulfilled at least 2 criteria: were selected if they answered at least 2 of the following criteria for both $\delta^{13}C$ and δ^2H: (i) $\chi(CH_4)$ above background > 90 ppb, (ii) Person coefficient r^2 of the linear fit > 0.75, and (ii) the standard deviation of the y-intercept lower than 5 ‰ for $\delta^{13}C$ and 100 ‰ for δ^2H respectively.

3 Results and discussion

3.1 Observed time series

The observed time series are shown in Fig. 2, together with measurements of CH_4 at Kasprowy Wierch. We note that in the period February-March 2019, we observed a mismatch of about 80 ppb between the IRMS-derived and simultaneous CRDS $\chi(CH_4)$ measurements in the same laboratory (shaded area in Fig. 2). A mismatch in mole fraction can potentially affect the Keeling plot intercepts, and we investigated possible artefacts using various attempts for correction. We realised that the effect of these corrections on the isotopic source signatures is small compared to the observed range (average peak $\delta^{13}C$ and δ^2H changed by 0.1 %; different peak source signatures are shown in Fig. S5.B). As no obvious reason for a malfunction of the IRMS instrument could be detected, we decided to use the original data without correction. The peaks in $\chi(CH_4)$, compared to the background measured at Kasprowy Wierch, reflect pollution events in Krakow or advected to the measurement site. The maximum $\chi(CH_4)$ value was 3634 ppb, measured on October 19th, 2018 at 5:30 am. Simultaneous changes are visible in the $\delta^{13}C$ and δ^2H time series. Increased $\chi(CH_4)$ were always linked with a lower δ^2H, but for $\delta^{13}C$ the measured values could be higher or lower.

The general background threshold is 1986.0 ppb, which corresponds to the 10th lower percentile of the entire dataset. We have found that 70.5 % of the background values ($\chi(CH_4) < 1986.0$ ppb) occurred during daytime. The dominant feature in the CH_4 time series is indeed the presence of a diurnal cycle: $\chi(CH_4)$ enhancements regularly occurred during the night. This is due to a lowering of the boundary layer when the temperature gradient decreases in the evening. The morning and evening variations in $\chi(CH_4)$ were negatively correlated with the temperature data we obtained at the study site. In addition, there were isolated pollution events occurring on top of the night-time accumulation. Between peaks, $\chi(CH_4)$ generally went back to a local background level.

The night-time accumulation was particularly visible in the period September 14th to mid-November 2018, and shown in the supplementary material (Fig. S2). Similar nighttime enhancements are also visible in the observations of other pollutants such as PM10 at the study location. There was a clear difference in local temperature before and after November 15, 2018: the average air temperature decreased from 12 ± 5.3 ℃ to 2.1 ± 4.4 ℃ and the dew point temperature from 5.3 ± 3.4 ℃ to -3.9 ± 3.4 ℃ until the end of the measurements. The period before mid-November will be referred to as fall throughout the paper.

The wind directions at the study site were combined with the CH_4 measurement data in Fig. 3; and with wind speeds in Fig. S3 of the supplementary material. The spread of the wind directions was similar for most of the months: mainly from the west (70 %), with a small contribution (27 %) from the east/northeast. An exception was November 2018, when most of the wind was from the east/north-east direction. March 2019 was characterised by winds from the west only, and at particularly strong speeds (on average 3.1 m/s, compared to 1.8 m/s for the other months; Fig. S3). The average CH_4 diurnal cycle, defined as the prominence of night peaks, was on average 334 ppb throughout the entire time period, but only of 195 ppb when the winds were > 2.5 m/s. This decrease in amplitude with higher wind speeds was not influenced by the direction of the wind. During fall, 84 % of the peaks were observed at night and associated with low wind speeds, which suggests the influence of local pollution sources, and a relatively low influence of the wind direction.

The average isotopic values of the background were δ^{13}C = -47.8 $\pm$ 0.1 ‰, and δ^2H = -89 $\pm$ 3 ‰. The CH$_4$ enhancements were associated with consistently more negative δ^2H, but varying δ^{13}C. This indicates that the sources were sometimes higher in δ^{13}C compared to the ambient CH$_4$ (i.e. δ^{13}C> -47.8 ‰). In contrast, all CH$_4$ enhancements were associated with lower δ^2H during the entire time period.

3.2 Modelled time series

The CH$_4$ time series obtained with CHIMERE for the grid cell containing the observation site, are shown in Fig. 4. We first compared the CH$_4$ mole fractions measured at Krakow and modelled by CHIMERE in Fig. 5. They show a poor correlation (Person's correlation coefficients r^2 = 0.527 and r^2 = 0.514, for model calculations using the EDGAR v5.0 and CAMS-REG-GHG v4.2 inventories, respectively; Fig. 5.A). The model globally under-estimates the measured χ(CH$_4$) significantly, with a root mean square error (RMSE) of 164.4 ppb and 173.4 ppb for EDGAR and CAMS, respectively. Yet we see that modelled χ(CH$_4$) can sometimes be larger than the observations, which is usually due to a shift in the timing of a pollution event (Fig. 4). The wind data used in the model are generally in good agreement with the wind measurements at the study site, but small discrepancies can partly explain the differences in the timing of the peaks. The time series are best reproduced during the fall 2018, using EDGAR v5.0 (r^2 = 0.648; Fig. 5.B). As mentioned in section 3.1, the fall of 2018 shows a more regular pattern of night-time enhancements of relatively similar amplitudes compared to the winter period. This is better reproduced by the model (Fig. 4). However, the two highest χ(CH$_4$) measurements were observed in this period (October 18, and November 3, 2018) and were not modelled to the same level (points on the lower right, Fig. 5.B). These events largely contribute to the general model under-estimation when only considering the fall data.

In winter, the χ(CH$_4$) enhancements were less regular, with a less consistent diurnal cycle (Fig. S2). The mismatch in the timing of pollution events caused an over-estimation by the model (points on the upper left, Fig. 5.B). The general slope is still lower than 1, and the fit is worse than during fall. There is a general under-estimation of the CH$_4$ mole fractions at Krakow by the model. This could be explained by the model time series being hourly averages, compared to the observations of sampled air. To account for this bias, we compared the model data with observations that are also averaged over a 1h window, and/or interpolated to the modelled times. This had no effect on the correlation coefficients, suggesting a minor impact of the temporal representation error. Another reason for the under-estimation of χ(CH$_4$) in CHIMERE could be the presence of potential CH$_4$ sources in the close surroundings of the laboratory. Such emissions could affect the measurements but not the model, where they are diluted over the 11 km grid cell. The misfit between modelled and observed χ(CH$_4$) could also be due to some errors in the transport modelling or insufficient emissions in the inventories. Szénási (2020) identified the emission inventories as the main source of discrepancies between CHIMERE results and measured time series at two other European locations. The implications on the two inventories are discussed in detail in section 3.4.

Time series of δ^{13}C and δ^2H in CH$_4$ show negative or positive excursions relative to the background, and are linked to χ(CH$_4$) peaks (Fig. 4). When using CAMS-REG-GHG v4.2, δ^{13}C and δ^2H are always negatively correlated with χ(CH$_4$). But when using the EDGAR v5.0 inventory, δ^{13}C values are closer to the background. The isotopic discrepancies will be analysed in detail in relation to the source partitioning in the inventories, and the signatures we assigned to each source in section 3.4.

3.3 Isotopic source signatures

A total of 126 and 157 peaks were identified in the δ^{13}C and δ^2H time series, respectively, and 114 peaks were measured commonly by both isotope lines. From the Keeling plot applied to each of the peaks, we obtained the source signatures of the corresponding accumulation events. They can be compared with the determined isotope signatures of the sources sampled in the surrounding area (Fig. 6.A).

3.3.1 Isotopic characterisation of the surrounding sources during mobile surveys

The results from 55 individual sites are presented in Table 2, and shown in detail in the supplementary material (Table S1 and Fig. S5.A). The maximal χ(CH$_4$) sampled at each location varied between 93 ppb above background and 95 % (pure gas), with a median of 1480 ppb above background. The derived isotopic signatures are in good agreement with the ranges defined for the different categories in the literature (Sherwood et al. (2017)). Biogenic sources (a landfill, 3 manholes and a cow barn) correspond to the acetate fermentation pathway, characterised by relatively depleted δ^{13}C ($<$ -50 ‰) and δ^2H ($<$ -275 ‰; Milkov and Etiope (2018)). The landfill CH$_4$ is isotopically more enriched than the cow barn. This can be due to an isotope fractionation from diffusion and oxidation in the soil layers (De Visscher (2004), Bakkaloglu et al. (2021)). The fossil fuel CH$_4$ emissions we sampled were from coal exploitation and use of natural gas. The natural gas distribution network was sampled outside of compressor stations, close to gas stations and supply valves in residential areas. The results ranged between [-52.3, -44.4] ‰ for δ^{13}C, and [-225, -177] ‰ for δ^2H. To check for temporal variations, 4 plumes were sampled at an interval of 6 weeks, on February 5 and March 19, 2019. The δ^{13}C results were about 4.7 ‰ more depleted, and the δ^2H were 27 ‰ more depleted in March compare to February. One sample was directly taken from the gas supply pipe at the AGH lab in March 2019. The pure gas was 3.6 ‰ and 14 ‰ more depleted in δ^{13}C and δ^2H, respectively, than the average from accidental leaks (signature in brackets in Table 2), which indicates that the isotopic composition of the city gas in March is relatively depleted compared to February. The network gas composition can change in time because the proportions of gas from several origins vary. Gas migrating in the distribution network can undergo secondary processes. For example CH$_4$ oxidation into CO$_2$ influences the isotopic signatures, usually towards more enriched values. Isotopic variations among network gas leaks were also observed previously in other cities (Zazzeri et al. (2017), Maazallahi et al. (2020), Defratyka et al. (2021)). The isotopic signature of the pure gas we sampled still falls in the same range as the sampled leaks.

CH$_4$ emissions from manholes were often observed in the Krakow urban area. The resulting isotopic signatures do not indicate one clear origin, and were divided in two groups with distinct δ^2H (Table 2). While the isotopically depleted signatures observed at 3 locations likely come from the sewage system, with a δ^2H $<$ -300 ‰, the 5 others contain CH$_4$ with particularly enriched δ^2H (between -202 and -146 ‰), not typical for microbial fermentation processes (Fig. S5.A). We hypothesise that this indicates leakage of natural gas from the distribution pipes to the sewage network, which is sometimes further oxidised leading to even more enriched isotope signatures.

For most emission plumes, we could not visually identify an obvious CH$_4$ source. The isotopic signatures of these "unknown" sources range from -58.2 to -34.9 ‰ V-PDB for δ^{13}C and from -285 to -142 ‰ V-SMOW for δ^2H. These large ranges in δ^{13}C

and δ^2H indicated the presence of both fossil fuel and biogenic sources. The average δ^2H is > 200 ‰, suggesting a major influence from fossil fuel sources. The δ^{13}C is in good agreement with the signature found for natural gas (Table 2 and Fig. S5.A), and since most of these locations were close to roads and urban settlements, it is likely that they were natural gas leaks.

The isotope signatures from coal mine ventilation shafts and residential gas leaks sampled in this study fall in the same range (Table 2 and Fig. 6.A): δ^{13}C between -59.8 and -28.1 ‰ V-PDB, and δ^2H between -254 and -152 ‰ V-SMOW, although coal CH$_4$ has a wider isotopic range. Values of δ^{13}C < -60 ‰ reported in the literature (Kotarba (2001), Kotarba and Pluta (2009) and Kedzior et al. (2013); Fig. S5.A) confirmed the presence of microbial gas in the USCB. Most δ^{13}C values from coal mines in this study were between -58 ‰ and -45 ‰, which also indicates a contribution from microbial gas sources, although in our measurements all δ^{13}C signatures from time series peaks and sampled shafts were > -60 ‰. Some of the locations sampled in by Kotarba (2001) were re-visited in this study. However, their method used direct sampling of CH$_4$ from different coal layers, aiming at representing the variety in the origin of the gas reservoirs. Our approach was to sample outside the shafts, to obtain the isotopic signature of CH$_4$ emissions from these shafts to the atmosphere. The very depleted δ^{13}C values obtained in these previous studies confirm the presence of purely microbial gas reservoirs in the USCB coal deposits, but our results show that thermogenic gas represents a larger part of the fugitive emissions from mining activities in this area than indicated by Kotarba (2001; Fig. 6.A). The heterogeneity of isotopic signatures from coal mining activities in the USCB reflects the geological complexity of the area. Secondary processes (desorption, diffusion or oxidation) also influence the CH$_4$ isotopic composition, and depend on external parameters such as physical characteristics of the coal reservoirs and the soil layers (Niemann and Whiticar (2017)). These represent additional difficulties which have to be taken into account in the isotopic characterisation of coal associated CH$_4$ emissions.

The δ^2H signatures allow us to identify the CH$_4$ emissions from microbial fermentation: values below -250 ‰ are indicative of the anaerobic fermentation pathway, such as in the rumen of cows or during waste degradation. Except for one shaft with δ^2H = -254 ± 1 ‰ (possibly very early mature thermogenic gas in deep formations, or a late stage of biodegradation if close to the surface; Milkov and Etiope (2018)), both literature data and our sampled shafts have a δ^2H > -250 ‰. This is also true for emissions from the natural gas network, confirming their fossil fuel origin. In the USCB region, δ^2H signatures seem to be more suitable than δ^{13}C values for source apportionment, similar to recent studies made in European cities (in Hamburg by Maazallahi et al., 2020, and in Bucharest by Fernandez et al., 2021)

3.3.2 Isotopic characterisation of CH$_4$ in ambient air

The isotopic signatures of the CH$_4$ pollution events observed in Krakow during the study period are shown in Fig. 6. δ^{13}C varied between -59.3 and -37.4 ‰ V-PDB, and δ^2H between -291 and -137 ‰ V-SMOW. As mentioned above, the observed δ^{13}C either increased or decreased with higher χ(CH$_4$), indicating source signatures either lower or higher than the background value. Yet δ^{13}C signatures stayed within ± 8 ‰ from the background, thus never reaching extreme values. There was 40.5 % of CH$_4$ peaks with a δ^{13}C more enriched than the background of -47.8 ‰. In contrast, the observed δ^2H values were always more depleted than ambient. The overall source signatures resulting from the Miller-Tans analysis using all the data points were δ^{13}C = -48.7 ± 0.0 ‰, and δ^2H = -205 ± 0 ‰ (Fig. S4). The comparison with typical signatures of the different CH$_4$

formation processes indicates that most of these events were from thermogenic sources (Fig. S5.B). When compared with isotope signatures of the surrounding sources (Fig. 6.A), the source signatures from the long-term time series match the range of coal mine and natural gas emissions the best. Fig. 6.B shows that most pollution events associated with strong winds fall in the range of more depleted δ^{13}C signatures. They were also all advected from west of Krakow, where the USCB is located (Fig. 1). In fact, the δ^2H signatures exclude a large contribution from potential biogenic sources, and point towards the emissions from coal mines in Silesia. CH$_4$ sources with the most enriched δ^{13}C mostly originated from the east, where the city centre and industrial areas are (Fig. 6.B). The Miller-Tans plots were also applied on the time series divided per wind sector (north-east, south-east, south-west and north-west; Fig. S4). The δ^{13}C source signature from north-east is more enriched compared to the other directions, with a value of -46.3 ± 0.3 ‰, and confirms the relative enrichment in δ^{13}C of CH$_4$ sources east of the study site.

In Röckmann et al. (2016) and Menoud et al. (2020b), CH$_4$ mole fractions, δ^{13}C and δ^2H isotopic signatures in ambient air were measured at two locations in the Netherlands. The time series covered 5 months in 2014-2015 and 2016-2017, at Cabauw and Lutjewad, respectively. The average isotopic signatures were -60.8 ± 0.2 ‰ and -298 ± 1 ‰ at Cabauw and -59.5 ± 0.1 ‰ and -287 ± 1 ‰ at Lutjewad, for δ^{13}C and δ^2H respectively. The main sources contributing to the CH$_4$ emissions in the Netherlands are cattle farming and waste management. These are biogenic sources, with isotopic signatures representative for the microbial fermentation origin. CH$_4$ of fossil fuel origin had a minor contribution there, which contrasts a lot with the results from Krakow. Such drastic differences in the isotopic signals of the same trace gas show how a region-specific analysis is crucial to effectively constrain atmospheric emissions.

In Fig. 7, the results of CH$_4$ mole fraction, peak source signatures and wind speed and direction are shown in more details for 8 days in November 2018, and 7 days in February 2019, together with model results using EDGAR v5.0. As mentioned previously, eastern winds generally advected CH$_4$ with a relatively enriched δ^{13}C: 60 % were higher than the background δ^{13}C, and all but one were > -50 ‰ V-PDB. In November, the wind was mostly coming from the east (Fig. 3), but enhancements were observed at low wind speed (Fig. 7.A, peaks 4 to 7). These pollution events reflect the general signature of the CH$_4$ emitted in the Krakow urban area and are unlikely to come from coal mines. In Fig. 7.A, the modelled peaks C, D, E and G show a large contribution from the natural gas and from the "other anthropogenic" categories. The latter represents mainly the power generation and transportation sectors, as well as the manufacture, chemical and metal industries. The main contribution is the energy production from fossil fuels, and we assigned a δ^{13}C signature corresponding to fossil fuel CH$_4$ to this category (Table 1). The modelled results for these peaks are generally similar to the measured ones. The magnitude of the χ(CH$_4$) enhancements also matches the observations relatively well: modelled peaks C, D, and E were 79 ppb, 23 ppb and 14 ppb larger than the observed peaks 3, 4 and 5, respectively. Yet for peak C (observed peak 3), the model δ^{13}C signature is 2.8 ‰ lower than the one from the measurements, and showed a majority of emissions from "other anthropogenic" sources (37 %). Part of these emissions can be from the incomplete combustion of CH$_4$, and such combustion-related emissions have a more enriched δ^{13}C signature than fossil fuel CH$_4$ (Fig. 6.A). Results from mobile surveys in Paris identified fuel-based residential heating systems as urban CH$_4$ sources, with a slightly more enriched isotopic composition than the local gas leaks (Defratyka et al. (2021)). Therefore, either the proportion of emissions in the "non-industrial combustion" category, or the δ^{13}C signature

assigned to the "other anthropogenic" emission category were under-estimated. We note that we couldn't characterise this source category by sampling. Uncertainties in the assigned signature are unavoidable when a given category is a combination of different sources; not only the processes have different isotopic signatures, but the contribution from the different sources could change from one pollution event to another. For δ^2H, the agreement between observed and modelled signatures for these November night peaks is good. All fossil fuel and pyrogenic δ^2H signatures used in this study are relatively close to each other (Table 1), and to the average peak δ^2H source signature. Thus, the δ^2H signatures do not allow for a distinction between these two processes.

Some peaks advected at low wind speeds during night are also visible in Fig. 7.B (peaks 9 to 11), and show similarly enriched δ^{13}C signatures. The wind direction was different for these night peaks between February and November, but the low wind speeds again indicate that this represents the local emission mix. The model time series showed peaks that occurred simultaneously to the measured ones (K and L in Fig. 7.B), although with different χ(CH$_4$) maxima than the measurements (-115, -339 and +203 ppb, respectively). For peaks K and L, the source partitioning from the inventory is similar to the other night peaks shown in Fig. 7.A. The δ^{13}C signatures of these urban emissions are however under-estimated in the model, and so are the CH$_4$ mole fractions, in particular for peak 11 (corresponding to peak L in the model time series). We suggest that at a close distance east of the study site, the share of emissions from the combustion sources is likely under-estimated. These additional emissions could be from residential heating or the energy production sector. The δ^2H signature of peak 11 (L) also differs significantly between model and measurements. This further indicates that the missing CH$_4$ emissions must be mostly combustion related, because of the relatively enriched δ^{13}C and δ^2H we observed (-44.2 $\pm$ 0.1 ‰ V-PDB and -198 $\pm$ 3 ‰ V-SMOW, respectively, for peak 11).

The δ^{13}C signatures shifted towards more depleted in heavy isotopes values after February 19. δ^{13}C went from -44.2 $\pm$ 0.1 ‰ for peak 11 to -49.8 $\pm$ 0.1 ‰ for peak 13. Peaks 12 and 13 (respectively M and N in the model), were advected by strong westerly winds. The share of coal related emissions reported in the inventory increased from peak M compared to peaks K and L, and is supported by the decrease in δ^{13}C also in the modelled signatures. This confirms a source shift from urban to coal activities further west of Krakow from February 19, 2019. Whenever the EDGAR inventory reported large contributions from coal mine emissions, such as in for peaks F, H, K, M and N (corresponding to 6a, 8, 10a, 12 and 13, respectively), the model wind direction corresponds to the USCB. The associated isotopic signatures were in relatively good agreement for peaks H, M, and N, where coal emissions represented > 50 % of the total. Small discrepancies (within 3 ‰ in δ^{13}C) are explained by the heterogeneity of isotopic signatures from the different mine shafts. This confirms that the average isotopic signatures for this category are well characterised in this study. For peaks F and K, δ^{13}C values are at least 2 ‰ lower than the observations (peaks 6a and 10a). The share of emissions from the USCB are therefore likely over-estimated in these 2 cases.

Seven peaks in the entire dataset showed a δ^2H < -255 ‰ V-SMOW, suggesting a larger contribution from biogenic sources (Fig. 6.A). They are associated with large uncertainties, because the peak magnitudes were low. These peaks were not modelled by CHIMERE, using either inventory. They represent isolated pollution events, disconnected from the daily cycle and not particularly related to a certain wind direction. There could be occasionally larger biogenic emissions such as from a waste facility that are advected to the measurement site. In Fig. 7.B, a depleted δ^2H signature was derived from a small peak (12a).

The $\chi(CH_4)$ enhancement was not significant in the time series of $\delta^{13}C$, which suggests a very short pollution event. It still correlated with a short-term change in wind direction towards a more north/north-west origin. Such abrupt changes are not visible in the model wind data, because of its coarser temporal resolution. Based on its clearly biogenic isotopic signal, as well as the wind direction, this event might reflect the contribution from the 2 large waste treatment facilities located north-west of Krakow (Fig. 1). This needs to be confirmed by observations at higher mole fractions to reduce the uncertainty in the source signature, and be able to derive a signature for $\delta^{13}C$, as we are reaching here our detection limit. Further measurements at this location would be useful to specifically characterise this source.

In addition to the night time accumulations of CH_4, we observed occasional $\chi(CH_4)$ peaks during the day, not linked to the night-time lowering of the boundary layer. CH_4 emissions coming from a specific location and advected by strong winds to the measurement site resulted in sharp peaks, such as peak 2 in Fig. 7.A, that are separate from the daily cycle. An increase in wind speed (from 0.7 to 2.2 m/s) and constant wind direction of 251 ° caused a sharp increase in $\chi(CH_4)$ by 1360 ppb, over only 3h. The peak was reproduced by the model (peak A), but with a lower magnitude, which can be explained by the differences in the wind data. The observed source signatures were δ^2H = -190 ± 9 ‰, indicating fossil fuel related emissions, and $\delta^{13}C$ = -49.3 ± 0.5 ‰, and correspond to localised coal mine fugitive emissions. The isotope signatures from the model using the EDGAR inventory differ significantly from the observed ones, even though coal extraction is still indicated as main source. The input source signatures in the model represent all coal related emissions and therefore might fail in reproducing the signature of emissions at the scale of individual sites.

3.4 CH_4 source partitioning in the inventories linked to isotopic composition

The CH_4 emissions for each source category from the inventories over the studied domain and the simulated CH_4 mole fractions in the grid-cell of the measurements location are presented in Table 3.

The modelled isotopic signatures when using CAMS-REG-GHG v4.2 inventory show that the CH_4 sources are always more isotopically depleted in $\delta^{13}C$ than when using EDGAR v5.0 (section 3.2, Fig. 4). When looking at the source partitioning between the 2 inventories, this can be explained by the much higher contribution from waste emissions when using the CAMS inventory (Table 3). These emissions have a particularly large influence at our study site (43.8 % of total added mole fraction), whereas the share in the emissions is not so large over the entire domain (26.2 % of total emissions). The emissions maps of both inventories are shown in Fig. S6 of the supplementary material. The higher waste emissions in CAMS-REG-GHG v4.2 are indeed coming from the Silesia region (Fig. S6). There is no evidence of particularly large amounts of domestic waste or waste collection facilities in this area. The Silesia and Krakow regions report comparable amounts of municipal waste per inhabitants, and in the same range as other regions of Poland (Statistics Poland, 2018). However, there are 5 times more waste from mining activities reported in Silesia than the other Polish regions (Statistics Poland, 2018). The emissions reported by CAMS are therefore associated with coal mining activities, especially mineral washing in the coal preparation plants. In our approach of distinguishing sources based on their isotopic signature, these emissions should be considered as fossil fuel related. However, in the CAMS inventory they are combined with waste emissions from the fermentation of organic substrate, which have a distinctly depleted isotope signature (Table 2, Fig. 6.A). The emissions from on-site energy use for coal mining and

for the manufacture of secondary and tertiary products from coal are included in the "other anthropogenic" category in both inventories (CRF sector 1.B.1.c, European Environment Agency (2019)). But in the EDGAR inventory, emissions categorised as from coal mining include fugitive emissions from the extraction and all the processing steps prior to combustion (CRF sector 1.B.1.a, European Environment Agency (2019)). They were therefore associated with the same signature as the coal extraction itself, which results in a better match with the observations than when using CAMS-REG-GHG v4.2.

The isotopic signatures per peak obtained from the model are compared with the ones from the observations in Fig. 8. The histograms show the distribution of isotopic signatures from the Keeling plots applied to each peak we extracted from the measured and modelled time series. The correlation plots allow to compare the CH_4 peaks detected simultaneously in the observed and modelled time series. When using the CAMS-REG-GHG v4.2 inventory, the $\delta^{13}C$ source signatures varied between -52.3 and -48.7 ‰, a much more narrow range than from -59.3 to -37.4 ‰ for the observations. This reflects the over-representation of the waste category and its associated depleted $\delta^{13}C$ signature. This bias towards depleted values is also visible in the δ^2H signatures. The source signatures when using the EDGAR v5.0 inventory match the observations better: the average $\delta^{13}C$ and δ^2H of all enhancements agree within their uncertainties, and the $\delta^{13}C$ signatures are slightly correlated (r^2=0.36). The distribution of $\delta^{13}C$ signatures with EDGAR has a bimodal shape that we also observe in the measured data, but covers a smaller range of values. Some of the most enriched signatures in the observations are not reproduced by the model, for both $\delta^{13}C$ and δ^2H (Fig. 8). As shown in Fig. 6.A, δ^2H allows to distinguish microbial fermentation from fossil fuel (or pyrogenic) sources, whereas the $\delta^{13}C$ ranges for these 2 source types overlap. This suggests that the fossil fuel fugitive and combustion-related emissions in the inventories are under-estimated. This mismatch is consistent with the lower $\chi(CH_4)$ in the model compared to the observations (Fig. 5), and is supported by our findings on the emission peak signatures (Fig. 7).

Finally, the absence of correlation between δ^2H signatures from model and observations (Fig. 8.B) emphasises the need for more δ^2H measurements in order to more precisely constrain the sources for this isotope signature. This limits the conclusions we could derive from measurements of δ^2H, especially in the context where δ^2H is particularly relevant for source attribution.

4   Conclusions

This study presents measurements of CH_4 mole fractions, $\delta^{13}C$ and δ^2H of CH_4 in ambient air, performed continuously during 6 months in 2018 - 2019 at Krakow, Poland. The results were combined with model simulations from a high-resolution regional transport model based on two different emission inventories.

The source signatures of the pollution events observed in Krakow were compared with signatures from sources sampled around the study area. This allows us to identify the fossil fuel-related sources as the main contributor to the CH_4 emissions. The wind directions pointed towards Silesian coal mines, but the use of natural gas in the urban area of Krakow is also an important source. Our results showed that despite the presence of microbial CH_4 reservoirs, CH_4 of thermogenic origin contributes the most to the atmospheric emissions from the USCB mine shafts. Despite their variability, the CH_4 isotopic signatures of Silesian coal mines are generally well constrained, and the overall emissions well characterised. The $\delta^{13}C$ source signature assigned to the USCB CH_4 emissions (-50.7 ‰ VPDB) agreed with the most recent estimate of -50.9 ‰ VPDB

by Gałkowski et al. (2020) (2020). However, the δ^2H source signatures were well reproduced when using a higher input δ^2H for coal mining emissions (-190 instead of -225 ‰ VSMOW). This study significantly helps constraining the CH$_4$ isotopic signatures from the USCB coal mining activities. Our isotopic observations when the wind was from the west at relatively high speeds confirm the prominence of coal-related CH$_4$ emissions compared to biogenic ones (agriculture and waste). The main

460 limitation of our approach in the context of Krakow is due to the overlap between the isotopic signatures form coal mines and natural gas, but could partly be overcome by a detailed analysis of the wind data.

In comparison to measurements made in the Netherlands (Röckmann et al. (2016), Menoud et al. (2020b)), the range of CH$_4$ isotopic signatures derived from the Krakow measurements was more enriched in δ^{13}C and δ^2H, by 10 ‰ and 100 ‰, respectively. These large differences are directly related to the heterogeneity in the human activities impacting our climate: from

465 agriculture (especially cattle farming) in the central Netherlands, to the exploitation of fossil fuels in south-western Poland. This provides additional evidence for the value that the analysis of isotopologues can have in constraining the local to regional methane budget.

The χ(CH$_4$) computed using both inventories matched the measurements relatively well (r^2=0.65 using EDGAR v5.0) during fall 2018. However, the agreement is less during the winter months (r^2=0.40), largely reflecting discrepancies in the timing of

470 the pollution events. The model also under-estimated the CH$_4$ levels by on average 170 ppb compared to the observations. The isotopic results suggest that increased emissions in the inventories must be of fossil fuel origin.

The average isotopic source signatures from the model using the EDGAR v5.0 inventory were in good agreement with the ones from the measurements, which confirms the predominance of fossil fuel emissions. Larger differences were observed on the level of individual peaks. Uncertainties remain because of the combination of different sources within one category in the

475 EDGAR v5.0 inventory. Small discrepancies between observed and modelled signatures are also due to the inherent diversity of isotopic signatures, even within one source category, like we observed when sampling the USCB mines. When multiple CH$_4$ sources contribute to the total χ(CH$_4$), as it was the case for the Krakow urban area, the uncertainties in the isotopic characterisation increase further. The CAMS-REG-GHG v4.2 inventory quantified waste emissions as the main contributor to the regional CH$_4$ emissions, but does not distinguish residential waste from waste associated with the processing of coal, which

480 resulted in a large bias towards isotopically depleted sources. Therefore, our method fails to assess in detail the performance of this inventory. Nevertheless we show the power of continuous isotope data for analysing CH$_4$ emission sources on monthly and daily scales, in a very detailed manner. These measurements can be used in future work to improve and validate inventories, and thus help target the mitigation to the right sources. It requires CH$_4$ sources to be characterised locally, and additional sampling campaigns in the city of Krakow would be required to better define the different sources and their isotopic composition,

485 especially targeting CH$_4$ emissions with enriched δ^{13}C (>-45 ‰).

Using δ^2H measurements in the identification of the sources was essential in this region, compared to δ^{13}C, as the δ^{13}C from coal mine activities and the network gas overlaps with CH$_4$ emitted from microbial sources such as waste. Yet our conclusions using δ^2H isotopes are restricted by the limited amount of δ^2H measurements available. Our δ^{13}C data generally support the recent re-evaluations of global δ^{13}C-CH$_4$ from fossil fuel sources towards less enriched values (Schwietzke et al. (2016)). The

490 data presented here were collected in an area that has been under-investigated in the past, compared to its importance for the

European CH_4 emissions. It is therefore an important contribution to studies on the global CH_4 budget. The high time resolution and temporal coverage of $\chi(CH_4)$, $\delta^{13}C$ and δ^2H in CH_4 provided by this data are also particularly helpful to evaluate transport models on regional and global scales.

Data availability. The data that support the findings of this study are openly available at https://doi.org/10.5281/zenodo.4548748, upon
495   request. It will be made open access once the article is published.

Author contributions. M.M., C.V. J.N. and J.B. performed the isotopic measurements. M.M., J.N. and M.S. performed the mobile surveys and sampling. M.M. and C.V. processed the experimental data. B.S. performed the model simulation. M.M. performed the analysis, drafted the manuscript and designed the figures. T.R. aided in interpreting the results and worked on the manuscript. J.N., B.S., I.P., and T.R., discussed the results and commented on the manuscript. J.N., I.P., P.B. and T.R. were involved in planning and supervised the work.

500   *Competing interests.* No competing interests apply for this work.

Acknowledgements. This work was supported by the ITN project Methane goes Mobile – Measurements and Modelling (MEMO[2]; https://h2020-memo2.eu/). This project has received funding from the European Union's Horizon 2020 research and innovation programme under the Marie Sklodowska-Curie grant agreement No 722479. We specially thank all the team members of the experimental physics lab of AGH for their support in the installation and maintenance of the IRMS system.
505   We acknowledge ECCAD (Emissions of atmospheric Compounds and Compilation of Ancillary Data) for the archiving and distribution of the data.

References

Bakkaloglu, S., Lowry, D., Fisher, R., France, J., Brunner, D., Chen, H., and Nisbet, E.: Quantification of Methane Emissions from UK Biogas Plants, Waste management, in-press, 2021.

510 Beck, V., Chen, H., Gerbig, C., Bergamaschi, P., Bruhwiler, L., Houweling, S., Röckmann, T., Kolle, O., Steinbach, J., Koch, T., Sapart, C. J., van der Veen, C., Frankenberg, C., Andreae, M. O., Artaxo, P., Longo, K. M., and Wofsy, S. C.: Methane Airborne Measurements and Comparison to Global Models during BARCA: METHANE IN THE AMAZON DURING BARCA, Journal of Geophysical Research: Atmospheres, 117, [15310], https://doi.org/10.1029/2011JD017345, 2012.

Boggs, P. T., Byrd, R. H., Rogers, J. E., and Schnabel, R. B.: User's Reference Guide for ODRPACK Version 2.01 Software for Weighted
515 Orthogonal Distance Regression, 1992.

Chen, Y., Lehmann, K. K., Peng, Y., Pratt, L., White, J., Cadieux, S., Sherwood Lollar, B., Lacrampe-Couloume, G., and Onstott, T.: Hydrogen Isotopic Composition of Arctic and Atmospheric CH_4 Determined by a Portable Near-Infrared Cavity Ring-Down Spectrometer with a Cryogenic Pre-Concentrator, Astrobiology, 16, 787–797, https://doi.org/10.1089/ast.2015.1395, 2016.

Crippa, M., Guizzardi, D., Muntean, M., Schaaf, E., Vullo, L., Solazzo, E., Monforti-Ferrario, F., Olivier, J., and Vignatti, E.: EDGAR v5.0
520 Greenhouse Gas Emissions, Tech. rep., European Commission, Joint Research Centre (JRC), 2019.

De Visscher, A.: Isotope Fractionation Effects by Diffusion and Methane Oxidation in Landfill Cover Soils, Journal of Geophysical Research, 109, D18 111, https://doi.org/10.1029/2004JD004857, 2004.

Defratyka, S. M., Paris, J.-D., Yver-Kwok, C., Fernandez, J. M., Korben, P., and Bousquet, P.: Mapping Urban Methane Sources in Paris, France, Environmental Science & Technology, p. acs.est.1c00859, https://doi.org/10.1021/acs.est.1c00859, 2021.

525 Etminan, M., Myhre, G., Highwood, E. J., and Shine, K. P.: Radiative Forcing of Carbon Dioxide, Methane, and Nitrous Oxide: A Significant Revision of the Methane Radiative Forcing: Greenhouse Gas Radiative Forcing, Geophysical Research Letters, 43, 12,614–12,623, https://doi.org/10.1002/2016GL071930, 2016.

European Environment Agency: Annual European Union Greenhouse Gas Inventory 1990-2017 and Inventory Report 2019, Submission under the United Nations Framework Convention on Climate Change and the Kyoto Protocol EEA/PUBL/2019/051, European Commission,
530 Copenhagen, Denmark, 2019.

Eyer, S., Tuzson, B., Popa, M. E., van der Veen, C., Röckmann, T., Rothe, M., Brand, W. A., Fisher, R., Lowry, D., Nisbet, E. G., Brennwald, M. S., Harris, E., Zellweger, C., Emmenegger, L., Fischer, H., and Mohn, J.: Real-Time Analysis of $\delta^{13}C$- and δD-CH_4 in Ambient Air with Laser Spectroscopy: Method Development and First Intercomparison Results, Atmospheric Measurement Techniques, 9, 263–280, https://doi.org/10.5194/amt-9-263-2016, 2016.

535 Fernandez, J. M., Maazallahi, H., France, J. L., Corbu, M., Menoud, M., Ardelean, M., Calcan, A., van der Veen, C., Röckmann, T., Fisher, R. E., Lowry, D., and Nisbet, E. G.: Something about Urban Methane Emissions in Bucharest, Romania, Atmospheric Environment, In preparation, 2021.

Fiehn, A., Kostinek, J., Eckl, M., Klausner, T., Gałkowski, M., Chen, J., Gerbig, C., Röckmann, T., Maazallahi, H., Schmidt, M., Korbeń, P., Nęcki, J., Jagoda, P., Wildmann, N., Mallaun, C., Bun, R., Nickl, A.-L., Jöckel, P., Fix, A., and Roiger, A.: Estimating CH_4, CO_2, and CO
540 Emissions from Coal Mining and Industrial Activities in the Upper Silesian Coal Basin Using an Aircraft-Based Mass Balance Approach, Atmospheric Chemistry and Physics Discussions, https://doi.org/10.5194/acp-2020-282, 2020.

Fortems-Cheiney, A., Pison, I., Dufour, G., Broquet, G., Berchet, A., Potier, E., Coman, A., Siour, G., and Costantino, L.: Variational Regional Inverse Modeling of Reactive Species Emissions with PYVAR-CHIMERE, Preprint, Atmospheric Sciences, https://doi.org/10.5194/gmd-2019-186, 2019.

545 Gałkowski, M., Jordan, A., Rothe, M., Marshall, J., Koch, F.-T., Chen, J., Agusti-Panareda, A., Fix, A., and Gerbig, C.: In Situ Observations of Greenhouse Gases over Europe during the CoMet 1.0 Campaign Aboard the HALO Aircraft, Preprint, Gases/In Situ Measurement/Instruments and Platforms, https://doi.org/10.5194/amt-2020-287, 2020.

Granier, C., D'Angiola, A., Denier van der Gon, H., and Kuenen, J.: Report on the Update of Anthropogenic Surface Emissions, MACC-II Deliverable Report D 22.1, TNO Department of Climate, Air and Sustainability, Utrecht, Netherlands, 2012.

550 Hoheisel, A., Yeman, C., Dinger, F., Eckhardt, H., and Schmidt, M.: An Improved Method for Mobile Characterisation of $\delta^{13}CH_4$ Source Signatures and Its Application in Germany, Atmospheric Measurement Techniques, 12, 1123–1139, https://doi.org/10.5194/amt-12-1123-2019, 2019.

IPCC: Climate Change 2013: The Physical Science Basis ; Working Group I Contribution to the Fifth Assessment Report of the Intergovernmental Panel on Climate Change, Cambridge Univ. Press, Cambridge, UK and New York, NY, USA, 2013.

555 IPCC: Global Warming of 1.5°C. An IPCC Special Report on the Impacts of Global Warming of 1.5°C above Pre-Industrial Levels and Related Global Greenhouse Gas Emission Pathways, in the Context of Strengthening the Global Response to the Threat of Climate Change, Sustainable Development, and Efforts to Eradicate Poverty, In Press, 2018.

Kedzior, S., Kotarba, M. J., and Pekała, Z.: Geology, Spatial Distribution of Methane Content and Origin of Coalbed Gases in Upper Carboniferous (Upper Mississippian and Pennsylvanian) Strata in the South-Eastern Part of the Upper Silesian Coal Basin, Poland, International 560 Journal of Coal Geology, 105, 24–35, https://doi.org/10.1016/j.coal.2012.11.007, 2013.

Keeling, C. D.: The Concentration and Isotopic Abundances of Carbon Dioxide in Rural and Marine Air, Geochimica et Cosmochimica Acta, 24, 277–298, 1961.

Kotarba, M. J.: Composition and Origin of Coalbed Gases in the Upper Silesian and Lublin Basins, Poland, Organic Geochemistry, 32, 163–180, https://doi.org/10.1016/S0146-6380(00)00134-0, 2001.

565 Kotarba, M. J. and Pluta, I.: Origin of Natural Waters and Gases within the Upper Carboniferous Coal-Bearing and Autochthonous Miocene Strata in South-Western Part of the Upper Silesian Coal Basin, Poland, Applied Geochemistry, 24, 876–889, https://doi.org/10.1016/j.apgeochem.2009.01.013, 2009.

Levin, I., Bergamaschi, P., Dörr, H., and Trapp, D.: Stable Isotopic Signature of Methane from Major Sources in Germany, Chemosphere, 26, 161–177, https://doi.org/10.1016/0045-6535(93)90419-6, 1993.

570 Luther, A., Kleinschek, R., Scheidweiler, L., Defratyka, S., Stanisavljevic, M., Forstmaier, A., Dandocsi, A., Wolff, S., Dubravica, D., Wildmann, N., Kostinek, J., Jöckel, P., Nickl, A.-L., Klausner, T., Hase, F., Frey, M., Chen, J., Dietrich, F., Nęcki, J., Swolkień, J., Fix, A., Roiger, A., and Butz, A.: Quantifying CH_4 Emissions from Hard Coal Mines Using Mobile Sun-Viewing Fourier Transform Spectrometry, Atmospheric Measurement Techniques, 12, 5217–5230, https://doi.org/10.5194/amt-12-5217-2019, 2019.

Maazallahi, H., Fernandez, J. M., Menoud, M., Zavala-Araiza, D., Weller, Z. D., Schwietzke, S., von Fischer, J. C., Denier van der Gon, 575 H., and Röckmann, T.: Methane Mapping, Emission Quantification, and Attribution in Two European Cities: Utrecht (NL) and Hamburg (DE), Atmospheric Chemistry and Physics, 20, 14 717–14 740, https://doi.org/10.5194/acp-20-14717-2020, 2020.

Mailler, S., Menut, L., Khvorostyanov, D., Valari, M., Couvidat, F., Siour, G., Turquety, S., Briant, R., Tuccella, P., Bessagnet, B., Colette, A., Létinois, L., Markakis, K., and Meleux, F.: CHIMERE-2017: From Urban to Hemispheric Chemistry-Transport Modeling, Geoscientific Model Development, 10, 2397–2423, https://doi.org/10.5194/gmd-10-2397-2017, 2017.

580   Menoud, M., Röckmann, T., Fernandez, J., Bakkaloglu, S., Lowry, D., Korben, P., Schmidt, M., Stanisavljevic, M., Necki, J., Defratyka, S., and Kwok, C. Y.: Mamenoud/MEMO2_isotopes: V8.1 Complete, https://doi.org/10.5281/ZENODO.4062356, 2020a.

Menoud, M., van der Veen, C., Scheeren, B., Chen, H., Szénási, B., Morales, R. P., Pison, I., Bousquet, P., Brunner, D., and Röckmann, T.: Characterisation of Methane Sources in Lutjewad, The Netherlands, Using Quasi-Continuous Isotopic Composition Measurements, Tellus B: Chemical and Physical Meteorology, 72, 1–19, https://doi.org/10.1080/16000889.2020.1823733, 2020b.

585   Menut, L., Bessagnet, B., Khvorostyanov, D., Beekmann, M., Blond, N., Colette, A., Coll, I., Curci, G., Foret, G., Hodzic, A., Mailler, S., Meleux, F., Monge, J.-L., Pison, I., Siour, G., Turquety, S., Valari, M., Vautard, R., and Vivanco, M. G.: CHIMERE 2013: A Model for Regional Atmospheric Composition Modelling, Geoscientific Model Development, 6, 981–1028, https://doi.org/10.5194/gmd-6-981-2013, 2013.

Milkov, A. V. and Etiope, G.: Revised Genetic Diagrams for Natural Gases Based on a Global Dataset of >20,000 Samples, Organic
590   Geochemistry, 125, 109–120, https://doi.org/10.1016/j.orggeochem.2018.09.002, 2018.

Miller, J. B. and Tans, P. P.: Calculating Isotopic Fractionation from Atmospheric Measurements at Various Scales, Tellus B: Chemical and Physical Meteorology, 55, 207–214, https://doi.org/10.3402/tellusb.v55i2.16697, 2003.

Monteil, G., Houweling, S., Dlugockenky, E. J., Maenhout, G., Vaughn, B. H., White, J. W. C., and Rockmann, T.: Interpreting Methane Variations in the Past Two Decades Using Measurements of CH_4 Mixing Ratio and Isotopic Composition, Atmospheric Chemistry and
595   Physics, 11, 9141–9153, https://doi.org/10.5194/acp-11-9141-2011, 2011.

National Centre for Emission Management (KOBiZe) and Institute of Environmental Protection - National Research Institute: Poland's National Inventory Report 2020 - Greenhouse Gas Inventory for 1988-2018, Tech. rep., Ministry of climate, Warsaw, Poland, 2020.

Necki, J. M., Chmura, Ł., Zimnoch, M., and Różański, K.: Impact of Emissions on Atmospheric Composition at Kasprowy Wierch Based on Results of Carbon Monoxide and Carbon Dioxide Monitoring, Polish Journal of Environmental Studies, 22, 1119–1127, 2013.

600   Niemann, M. and Whiticar, M.: Stable Isotope Systematics of Coalbed Gas during Desorption and Production, Geosciences, 7, 43, https://doi.org/10.3390/geosciences7020043, 2017.

Nisbet, E. G., Dlugokencky, E. J., Manning, M. R., Lowry, D., Fisher, R. E., France, J. L., Michel, S. E., Miller, J. B., White, J. W. C., Vaughn, B., Bousquet, P., Pyle, J. A., Warwick, N. J., Cain, M., Brownlow, R., Zazzeri, G., Lanoisellé, M., Manning, A. C., Gloor, E., Worthy, D. E. J., Brunke, E.-G., Labuschagne, C., Wolff, E. W., and Ganesan, A. L.: Rising Atmospheric Methane: 2007-2014 Growth and Isotopic
605   Shift: RISING METHANE 2007-2014, Global Biogeochemical Cycles, 30, 1356–1370, https://doi.org/10.1002/2016GB005406, 2016.

Nisbet, E. G., Manning, M. R., Dlugokencky, E. J., Fisher, R. E., Lowry, D., Michel, S. E., Myhre, C. L., Platt, S. M., Allen, G., Bousquet, P., Brownlow, R., Cain, M., France, J. L., Hermansen, O., Hossaini, R., Jones, A. E., Levin, I., Manning, A. C., Myhre, G., Pyle, J. A., Vaughn, B. H., Warwick, N. J., and White, J. W. C.: Very Strong Atmospheric Methane Growth in the 4 Years 2014–2017: Implications for the Paris Agreement, Global Biogeochemical Cycles, 33, 318–342, https://doi.org/10.1029/2018GB006009, 2019.

610   Pataki, D. E., Ehleringer, J. R., Flanagan, L. B., Yakir, D., Bowling, D. R., Still, C. J., Buchmann, N., Kaplan, J. O., and Berry, J. A.: The Application and Interpretation of Keeling Plots in Terrestrial Carbon Cycle Research: APPLICATION OF KEELING PLOTS, Global Biogeochemical Cycles, 17, 1022, https://doi.org/10.1029/2001GB001850, 2003.

Quay, P., Stutsman, J., Wilbur, D., Snover, A., Dlugokencky, E., and Brown, T.: The Isotopic Composition of Atmospheric Methane, Global Biogeochemical Cycles, 13, 445–461, https://doi.org/10.1029/1998GB900006, 1999.

615   Rigby, M., Manning, A. J., and Prinn, R. G.: The Value of High-Frequency High-Precision Methane Isotopologue Measurements for Source and Sink Estimation: Methane Isotopologues in Inversions, Journal of Geophysical Research: Atmospheres, 117, 1–14, https://doi.org/10.1029/2011JD017384, 2012.

Ringeval, B., Friedlingstein, P., Koven, C., Ciais, P., de Noblet-Ducoudré, N., Decharme, B., and Cadule, P.: Climate-CH$_4$ Feedback from Wetlands and Its Interaction with the Climate-CO$_2$ Feedback, Biogeosciences, 8, 2137–2157, https://doi.org/10.5194/bg-8-2137-2011, 2011.

Röckmann, T., Eyer, S., van der Veen, C., Popa, M. E., Tuzson, B., Monteil, G., Houweling, S., Harris, E., Brunner, D., Fischer, H., Zazzeri, G., Lowry, D., Nisbet, E. G., Brand, W. A., Necki, J. M., Emmenegger, L., and Mohn, J.: In Situ Observations of the Isotopic Composition of Methane at the Cabauw Tall Tower Site, Atmospheric Chemistry and Physics, 16, 10 469–10 487, https://doi.org/10.5194/acp-16-10469-2016, 2016.

Saunois, M., Stavert, A. R., Poulter, B., Bousquet, P., Canadell, J. G., Jackson, R. B., Raymond, P. A., Dlugokencky, E. J., Houweling, S., Patra, P. K., Ciais, P., Arora, V. K., Bastviken, D., Bergamaschi, P., Blake, D. R., Brailsford, G., Bruhwiler, L., Carlson, K. M., Carrol, M., Castaldi, S., Chandra, N., Crevoisier, C., Crill, P. M., Covey, K., Curry, C. L., Etiope, G., Frankenberg, C., Gedney, N., Hegglin, M. I., Höglund-Isaksson, L., Hugelius, G., Ishizawa, M., Ito, A., Janssens-Maenhout, G., Jensen, K. M., Joos, F., Kleinen, T., Krummel, P. B., Langenfelds, R. L., Laruelle, G. G., Liu, L., Machida, T., Maksyutov, S., McDonald, K. C., McNorton, J., Miller, P. A., Melton, J. R., Morino, I., Müller, J., Murguia-Flores, F., Naik, V., Niwa, Y., Noce, S., O'Doherty, S., Parker, R. J., Peng, C., Peng, S., Peters, G. P., Prigent, C., Prinn, R., Ramonet, M., Regnier, P., Riley, W. J., Rosentreter, J. A., Segers, A., Simpson, I. J., Shi, H., Smith, S. J., Steele, L. P., Thornton, B. F., Tian, H., Tohjima, Y., Tubiello, F. N., Tsuruta, A., Viovy, N., Voulgarakis, A., Weber, T. S., van Weele, M., van der Werf, G. R., Weiss, R. F., Worthy, D., Wunch, D., Yin, Y., Yoshida, Y., Zhang, W., Zhang, Z., Zhao, Y., Zheng, B., Zhu, Q., Zhu, Q., and Zhuang, Q.: The Global Methane Budget 2000–2017, Earth System Science Data, 12, 1561–1623, https://doi.org/10.5194/essd-12-1561-2020, 2020.

Schaefer, H., Fletcher, S. E. M., Veidt, C., Lassey, K. R., Brailsford, G. W., Bromley, T. M., Dlugokencky, E. J., Michel, S. E., Miller, J. B., Levin, I., Lowe, D. C., Martin, R. J., Vaughn, B. H., and White, J. W. C.: A 21st-Century Shift from Fossil-Fuel to Biogenic Methane Emissions Indicated by ^{13}CH$_4$, Science, 352, 80–84, https://doi.org/10.1126/science.aad2705, 2016.

Schwietzke, S., Sherwood, O. A., Bruhwiler, L. M. P., Miller, J. B., Etiope, G., Dlugokencky, E. J., Michel, S. E., Arling, V. A., Vaughn, B. H., White, J. W. C., and Tans, P. P.: Upward Revision of Global Fossil Fuel Methane Emissions Based on Isotope Database, Nature, 538, 88–91, https://doi.org/10.1038/nature19797, 2016.

Sherwood, O. A., Schwietzke, S., Arling, V. A., and Etiope, G.: Global Inventory of Gas Geochemistry Data from Fossil Fuel, Microbial and Burning Sources, Version 2017, Earth System Science Data, 9, 639–656, https://doi.org/10.5194/essd-9-639-2017, 2017.

Sperlich, P., Uitslag, N. A. M., Richter, J. M., Rothe, M., Geilmann, H., van der Veen, C., Röckmann, T., Blunier, T., and Brand, W. A.: Development and Evaluation of a Suite of Isotope Reference Gases for Methane in Air, Atmospheric Measurement Techniques, 9, 3717–3737, https://doi.org/10.5194/amt-9-3717-2016, 2016.

Statistics Poland: Chapter 6 - Odpady (Waste), in: Statistical Yearbook of the Republic of Poland, 2018, Dominik Rozkrut, Statistical Publishing Establishment, Warsaw, Poland, 2018.

Swolkień, J.: Polish Underground Coal Mines as Point Sources of Methane Emission to the Atmosphere, International Journal of Greenhouse Gas Control, 94, 102 921, https://doi.org/10.1016/j.ijggc.2019.102921, 2020.

Szénási, B.: Atmospheric Monitoring of Methane Emissions at the European Scale, PhD thesis, Université Paris-Saclay, 2020.

Tarasova, O., Brenninkmeijer, C., Assonov, S., Elansky, N., Rockmann, T., and Brass, M.: Atmospheric CH4 along the Trans-Siberian Railroad (TROICA) and River Ob: Source Identification Using Stable Isotope Analysis, Atmospheric Environment, 40, 5617–5628, https://doi.org/10.1016/j.atmosenv.2006.04.065, 2006.

620

625

630

635

640

645

650

655 Townsend-Small, A., Botner, E. C., Jimenez, K. L., Schroeder, J. R., Blake, N. J., Meinardi, S., Blake, D. R., Sive, B. C., Bon, D., Crawford, J. H., Pfister, G., and Flocke, F. M.: Using Stable Isotopes of Hydrogen to Quantify Biogenic and Thermogenic Atmospheric Methane Sources: A Case Study from the Colorado Front Range: Hydrogen Isotopes in the Front Range, Geophysical Research Letters, 43, 11,462–11,471, https://doi.org/10.1002/2016GL071438, 2016.

Turner, A. J., Frankenberg, C., and Kort, E. A.: Interpreting Contemporary Trends in Atmospheric Methane, Proceedings of the National
660 Academy of Sciences, 116, 2805–2813, https://doi.org/10.1073/pnas.1814297116, 2019.

Worden, J. R., Bloom, A. A., Pandey, S., Jiang, Z., Worden, H. M., Walker, T. W., Houweling, S., and Röckmann, T.: Reduced Biomass Burning Emissions Reconcile Conflicting Estimates of the Post-2006 Atmospheric Methane Budget, Nature Communications, 8, 2227, https://doi.org/10.1038/s41467-017-02246-0, 2017.

Yacovitch, T. I., Daube, C., and Herndon, S. C.: Methane Emissions from Offshore Oil and Gas Platforms in the Gulf of Mexico, Environ-
665 mental Science & Technology, 54, 3530–3538, https://doi.org/10.1021/acs.est.9b07148, 2020.

Zazzeri, G., Lowry, D., Fisher, R. E., France, J. L., Lanoisellé, M., Grimmond, C. S. B., and Nisbet, E. G.: Evaluating Methane Inventories by Isotopic Analysis in the London Region, Scientific Reports, 7, 4854, https://doi.org/10.1038/s41598-017-04802-6, 2017.
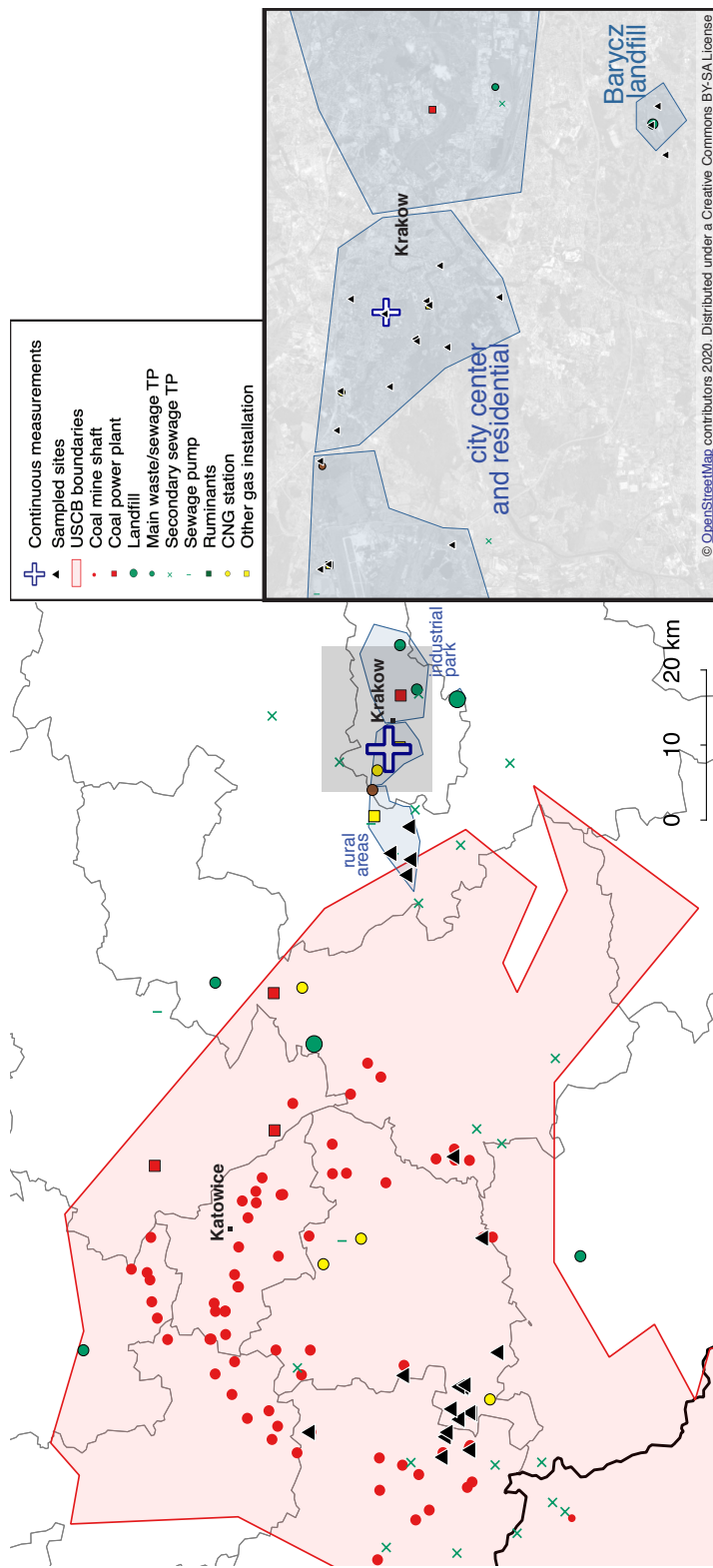
Figure 1. Location of the long-time measurements, sampled sites and potential anthropogenic methane sources. Note that this is not an exhaustive list: not all the sewage pumps are reported, and no official information on cattle farms was obtained. Other emissions from mining activities, coming from processing facilities or waste disposal, are not reported here. No $\chi(CH_4)$ enhancements were measured around stagnant water bodies, therefore they are not all reported here. ("TP" = treatment plant, "CNG" = compressed natural gas).
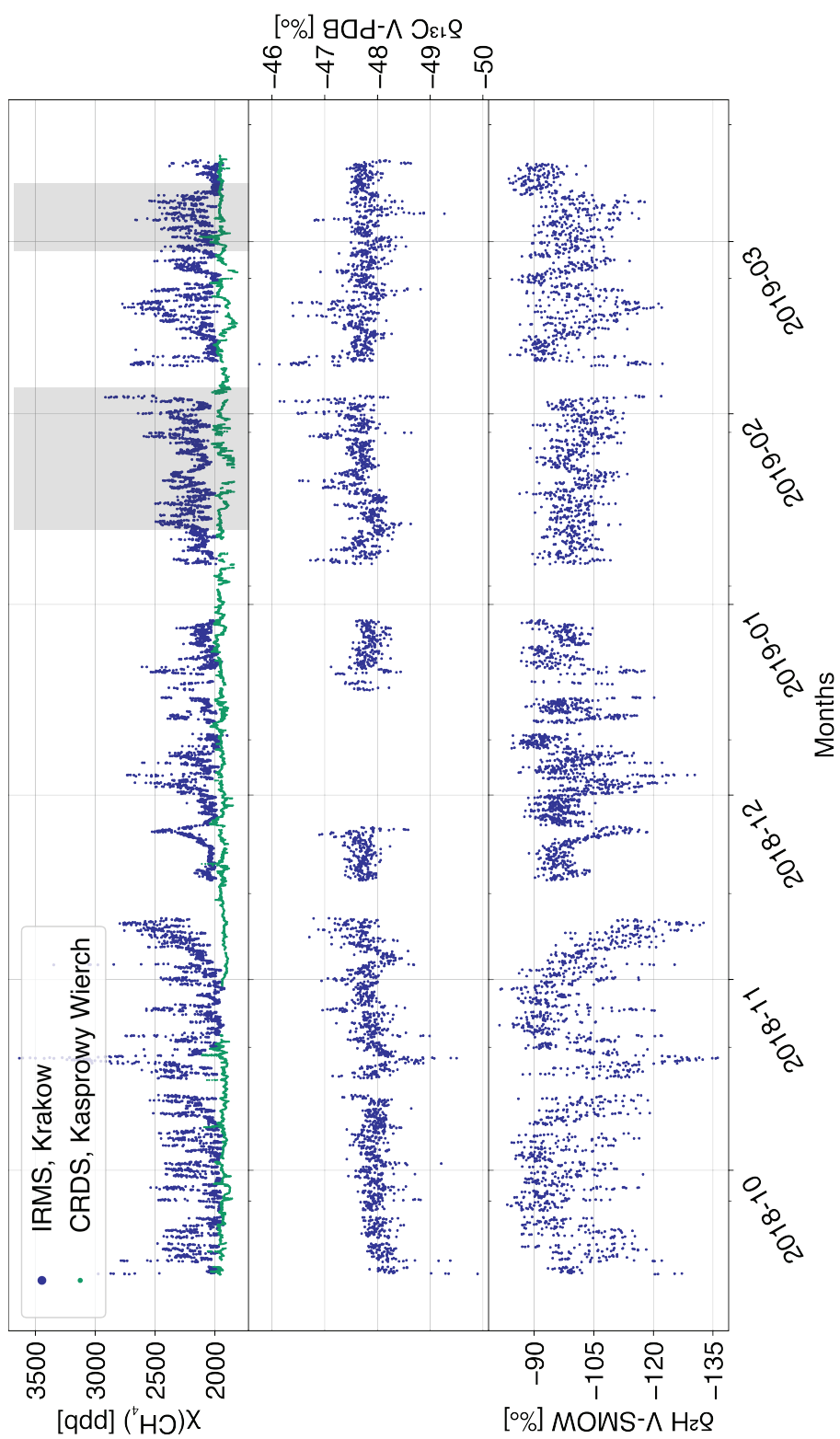
Figure 2. Time series of the observed $\chi(CH_4)$ (n=7886), $\delta^{13}C$ (n=3477), and δ^2H (n=4389), together with the $\chi(CH_4)$ time series observed at Kasprowy Wierch (green; n=21028). The shaded areas show when there was a mismatch between the IRMS and CRDS instruments in the mole fractions.
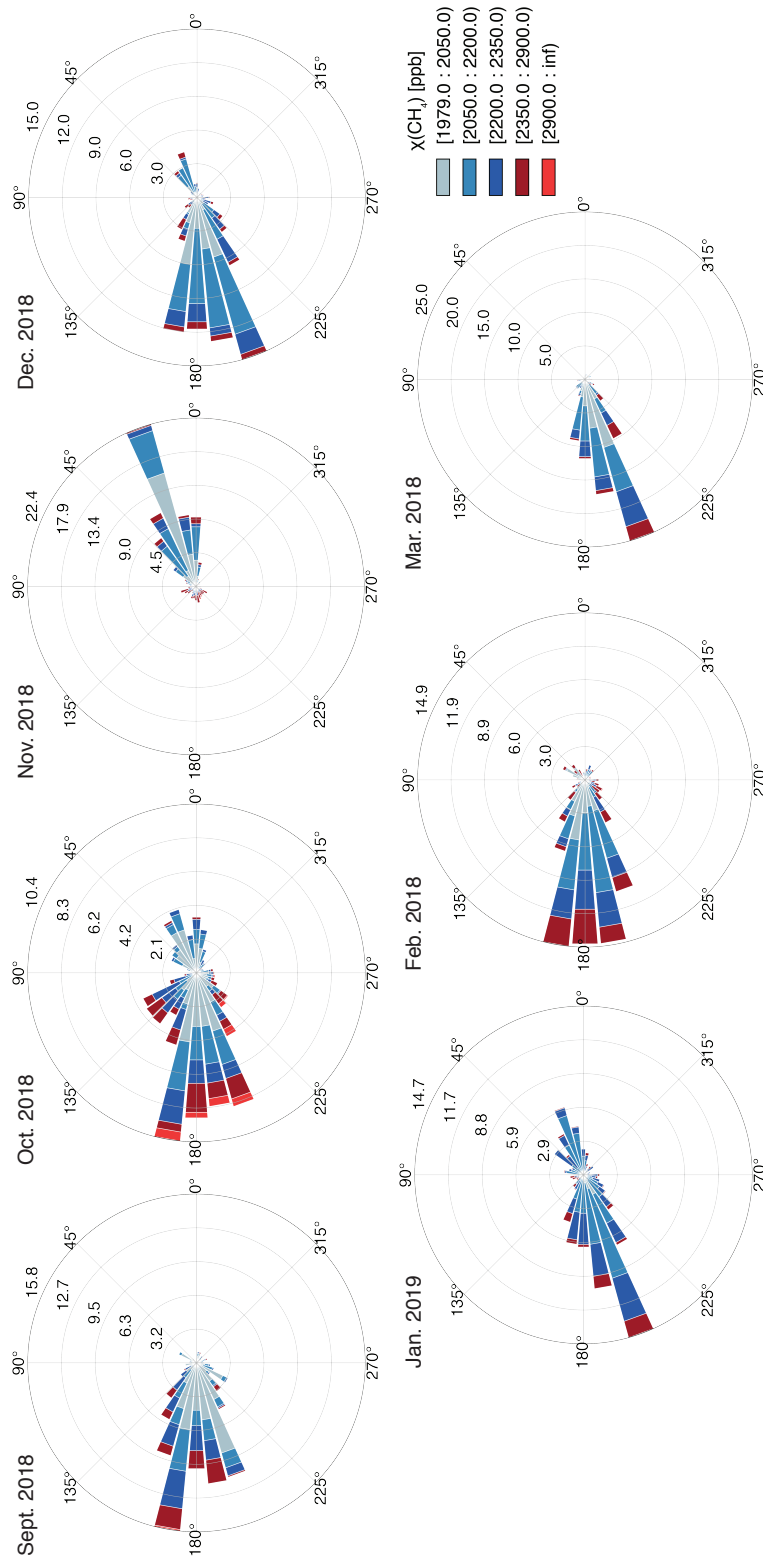
Figure 3. Monthly wind directions during the ambient air measurement period, at the same location. Bar lengths are percentages of records during the specified month (r-axis); colours define the $\chi(CH_4)$ range (legend).
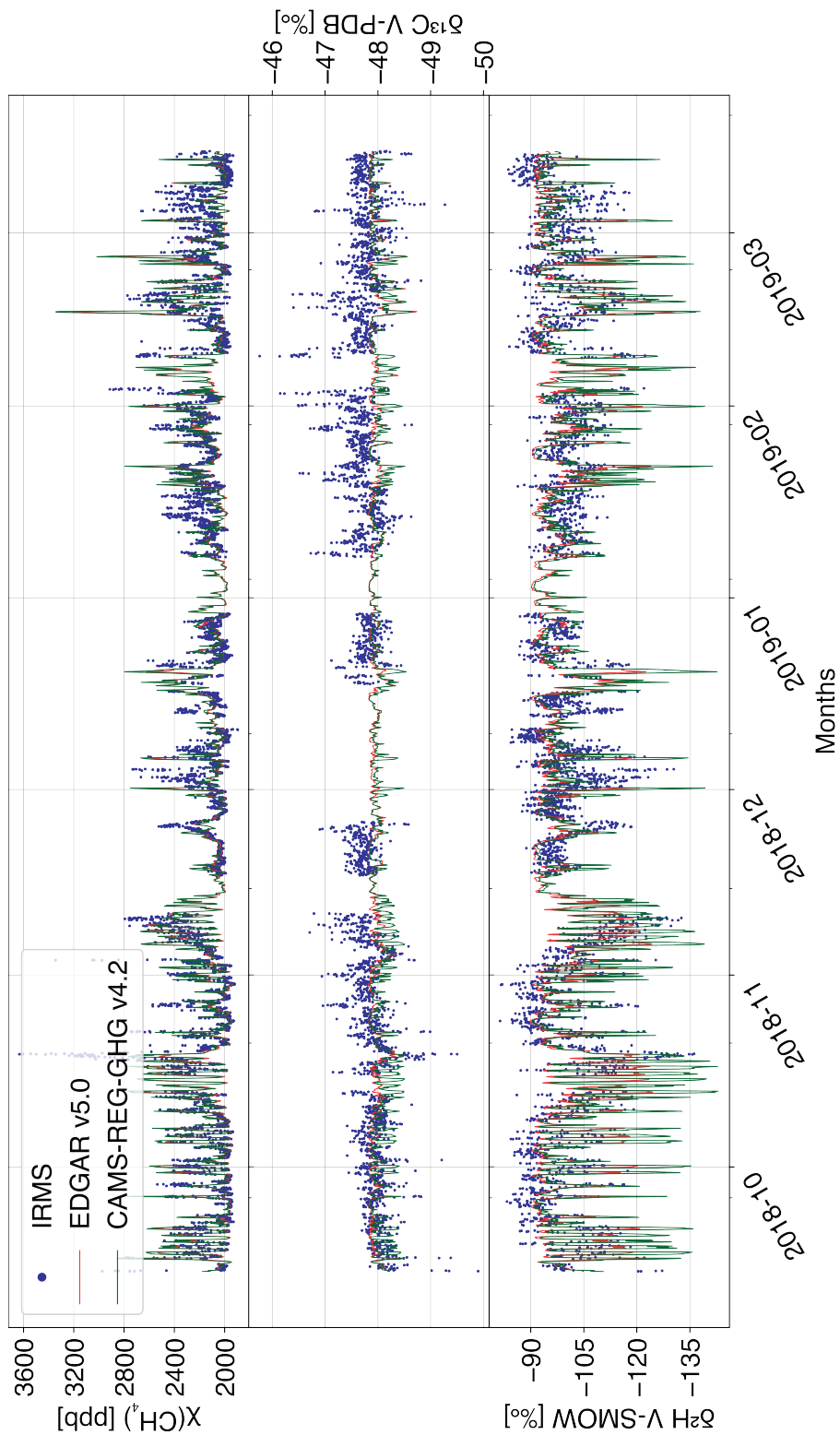
Figure 4. Time series of the observed (blue circles) and modelled $\chi(CH_4)$, $\delta^{13}C$ and δ^2H, based on the EDGAR v5.0 (red) and CAMS-REG-GHG v4.2 (green) inventories.
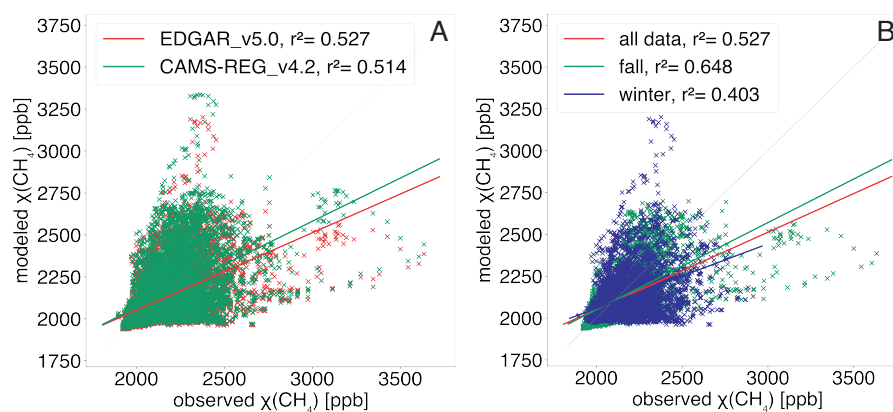
Figure 5. Correlation between observed and modelled $\chi(CH_4)$ values, using (a) the EDGAR v5.0 (red) or the CAMS-REG-GHG v4.2 (green) inventories, and (b) different time periods: fall (September 14 to November 15, 2018; green) or winter (November 15, 2018 to March 15, 2019; blue) computed using EDGAR v5.0.
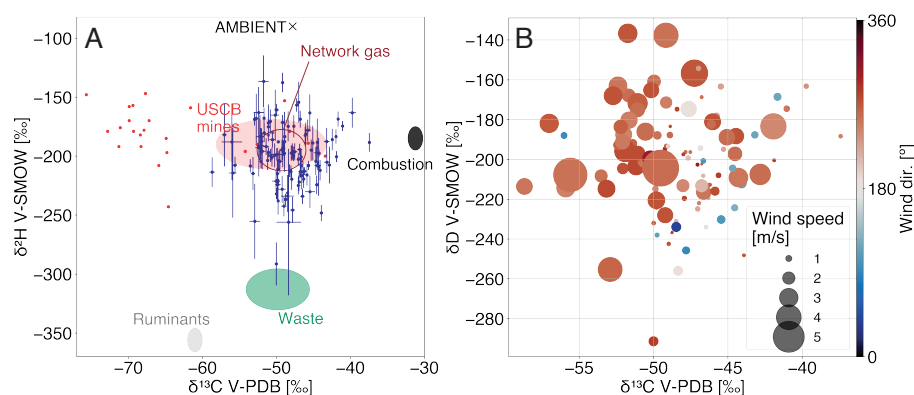
Figure 6. Dual isotope plots of the resulting source signatures from the CH_4 peaks identified in the time series. (a) Dark blue: source signatures with their associated 1σ uncertainties. Coloured areas: ranges of source signatures obtained from the collected samples. If based on 1 location (ruminants and combustion), the size of the ellipse is 1 order of magnitude the precision of our isotopic measurements. Red dots: source signatures of USCB coal gas derived from Kotarba (2001), Kotarba and Pluta (2009) and Kedzior et al. (2013). The combustion source signature is from coal waste burning samples reported in Menoud et al. (2020a). (b) Source signatures labeled by the average wind direction (colour) and speed (size) measured during the pollution event.
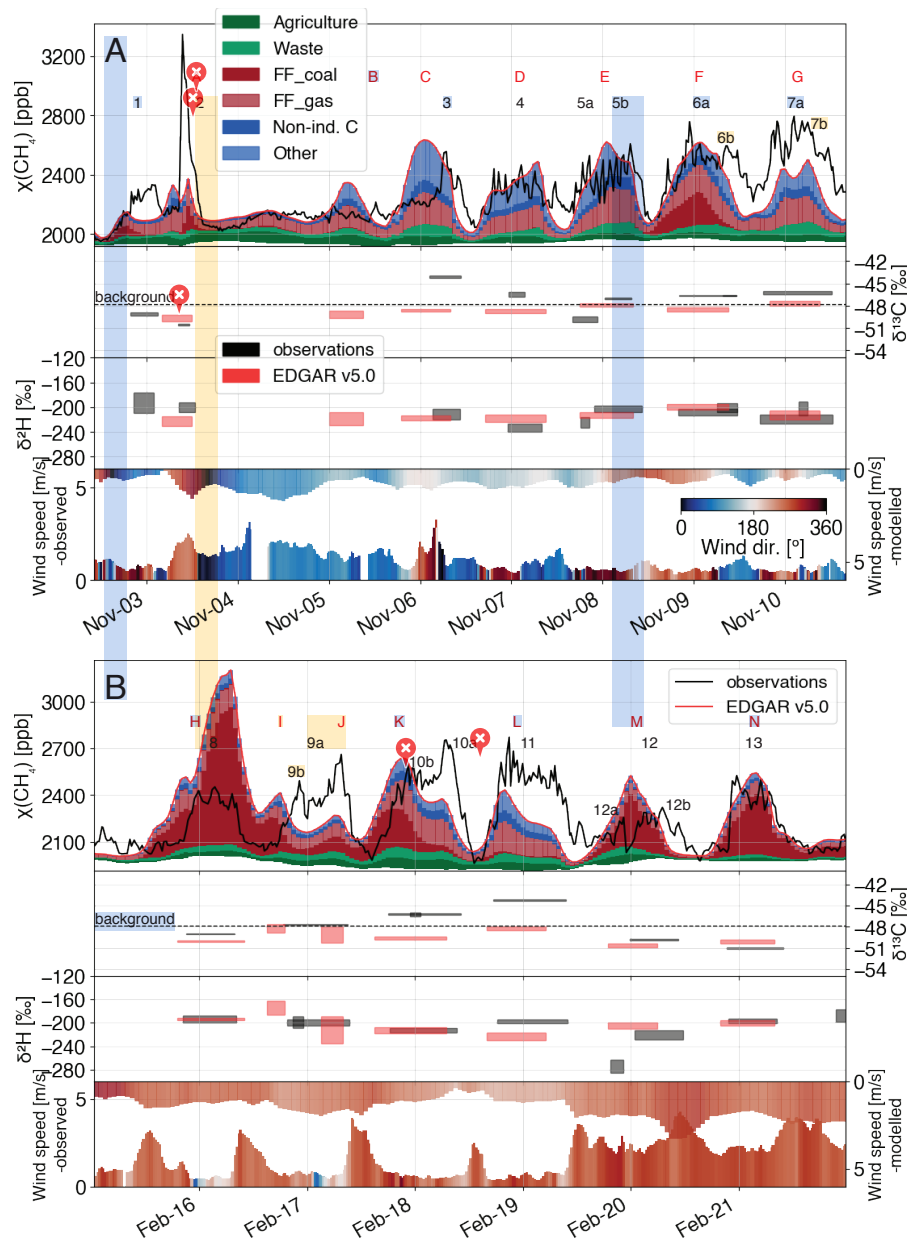
Figure 7. Detailed analysis of two subsets of the dataset, (a) from Nov. 2 to 10, 2018, (b) from Feb. 15 to 22, 2019. Top panels: observed (grey) and modelled (red) mole fractions and relative source contributions from the EDGAR v5.0 inventory. FF=Fossil fuel, Non-ind. C: Non-industrial combustion. Middle panels: $\delta^{13}C$ and δ^2H source signatures of individual peaks of the observed (grey, from peak 1 to 13) and modelled (red, from peak A to N) time series. Box heights represent $\pm 1\sigma$ of each peak isotopic signature. Bottom panels: wind speed and direction measured simultaneously at the study site (pointing up), and used for the CHIMERE simulations (pointing down).
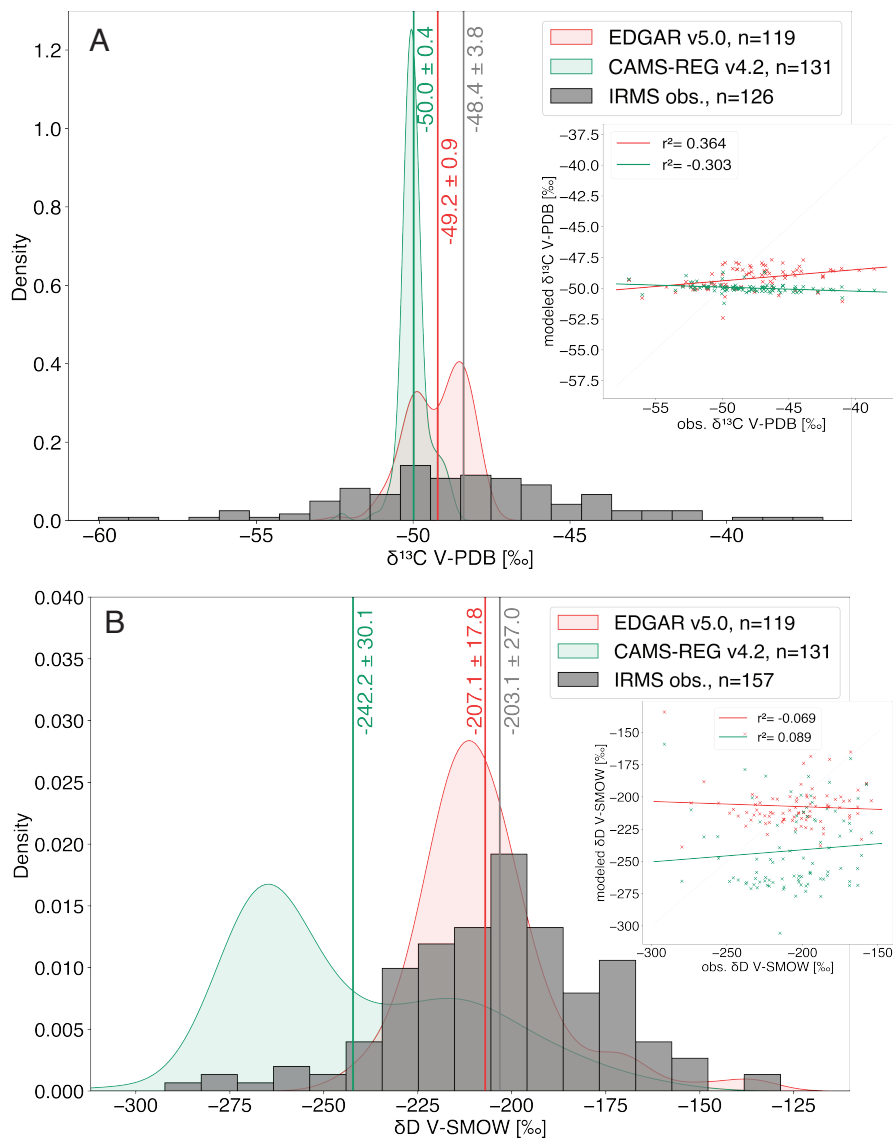
Figure 8. Distribution of source signatures of all peaks, and in the inset the correlation between modelled and observed ones. The vertical lines show the average values of each distribution ($\pm 1\sigma$). (a) δ^{13}C signatures in the observed (grey, n=126), modelled using EDGAR v5.0 (red, n=119) and modelled using CAMS-REG-GHG v4.2 (green, n=131) time series. (b) δ^2H signatures in the observed (grey, n=157), modelled using EDGAR v5.0 (red, n=119) and modelled using CAMS-REG-GHG v4.2 (green, n=131) time series.

Table 1. Methane emission categories considered for this study, with the corresponding classification in the inventories, and the respective isotopic signature used to compute δ^{13}C and δ^{2}H time series with CHIMERE. If no references are specified, the assigned isotope values are derived from the sampling campaigns we carried out in the study area and described in this paper.

CHIMERE source category	CRF sector[1]	IPCC 2006 code	EDGAR v5.0 sector	CAMS-REG-GHG v4.2 sector	Assigned δ^{13}C V-PDB [‰]	Assigned δ^{2}H V-SMOW [‰]
Agriculture	3 Agriculture	3A1 / 3A2 / 3C1b / 3C2, 3C3, 3C4, 3C7	Enteric fermentation / Manure management / Agriculture waste burning / Agriculture soils	K Agriculture -livestock / L Agriculture -other	-61.5	-356
Waste	5 Waste	4A, 4B / 4C / 4D	Solid waste landfills / Solid waste incineration / Waste water handling	J Waste	-51.3	-308
Fossil fuels	1B Energy - Fugitive emissions from fuels[2]	1B1a / 1B2bi, 1B2bii / 1B2aiii2, 1B2aiii3	Fuel explotation, coal / Fuel explotation, gas / Fuel explotation, oil	D Fugitives	-50.7 / -49.3 / -49.8	-190 / -195 / -193
Non-industrial combustion	1A4, 1A5 Energy - Other sectors, Other[2]	1A4, 1A5	Energy for buildings	C Other stationary combustion	-32.1[3]	-185[3]
Other anthropogenic	1A Energy - Industries	1A1a / 1A1b, 1A1ci, 1A1cii, 1A5biii, 1B1b, 1B2aiii6, 1B2biii3, 1B1c / 1A2	Power industry / Oil refineries and transformation industry / Combustion for manufacturing	A Public power		-193
	2 Industrial processes and product use	5B / 2B / 2C1, 2C2 / 2D3, 2E, 2F, 2G	Fossil fuel fires / Chemical processes / Iron and steel production / Solvents and products use	B Industry / E Solvents	-49.8	
	1A3 Energy - Transport	1A3b / 1A3d / 1A3a / 1A3c, 1A3e	Road transportation / Shipping / Aviation / Railways, pipelines, off-road transport	F Road transport / G Shipping / H Aviation / I Off-road		
Wetlands					-73.2[3]	-323[3]
Background					-47.8	-89

[1] European Environment Agency (2019)

[2] Mostly the use of coal for heating households (European Environment Agency (2019))

[3] Menoud et al. (2020ab)

Table 2. Isotope signatures of the different sources sampled in the region surrounding the study site. The values were used as input in the CHIMERE model.

Source type	Number of sites	Mean δ^{13}C V-PDB [‰]	1σ	Mean δ^{2}H V-SMOW [‰]	1σ
Coal mine	14	-50.7	7.5	-190	24
Cow barn	1	-61.5		-356	
Landfill	2	-55.0	1.5	-277	24
Manhole[1]	8 (5/3)	-44.9 (-42.5/-48.9)	9.0 (10.8/3.1)	-234 (-177/-328)	80 (23/11)
Network gas	7 (1)	-49.3 (-52.0)	3.3 (-)	-195 (-205)	18 (-)
Unknown	22	-48.0	4.8	-201	34

[1] Any hole in a road covered by a metal plate that can usually be removed.

Table 3. Methane absolute emissions and contributions of the different source categories used in CHIMERE to the total simulated $\chi(CH_4)$, for the EDGAR v5.0 and CAMS-REG-GHG v4.2 inventories.

	Emissions over domain [TgCH$_4$/yr]		Contribution at Krakow [ppb/ppb]	
Source categories	EDGAR v5.0	CAMS-REG-GHG v4.2	EDGAR v5.0	CAMS-REG-GHG v4.2
Agriculture	2.02	1.64	0.168	0.114
Waste	1.88	1.22	0.142	0.438
Fossil fuels - coal	0.52	-	0.145	
Fossil fuels - gas	1.23	-	0.309	
Fossil fuels - oil	0.02	-	0.00226	
Fossil fuels - total	1.77	1.32	0.456	0.346
Non-industrial combustion/Energy for buildings	0.31	0.28	0.0986	0.0667
Other anthropogenic	0.09	0.16	0.118	0.0201
Wetlands	0.4		0.0178	0.0157
Total	6.07	4.64	1	1

Compare Results

Old File:		New File:
KRK_supplementary-material_20210713.pdf	versus	**KRK_supplementary-material.pdf**
8 pages (8.00 MB)		**6 pages (11.58 MB)**
13/07/2021, 18:47:55		22/02/2021, 15:32:48

Total Changes

23

Text only comparison

Content

13 Replacements

4 Insertions

6 Deletions

Styling and Annotations

0 Styling

0 Annotations

Go to First Change (page 1)

Supplementary material

Title:

Methane (CH_4) sources in Krakow, Poland: insights from isotope analysis

Authors:

Malika Menoud, Carina van der Veen, Jaroslaw Necki, Jakub Bartyzel, Barbara Szénási, Mila Stanisavl-jević, Isabelle Pison, Philippe Bousquet, and Thomas Röckmann

Correspondance: m.menoud@uu.nl
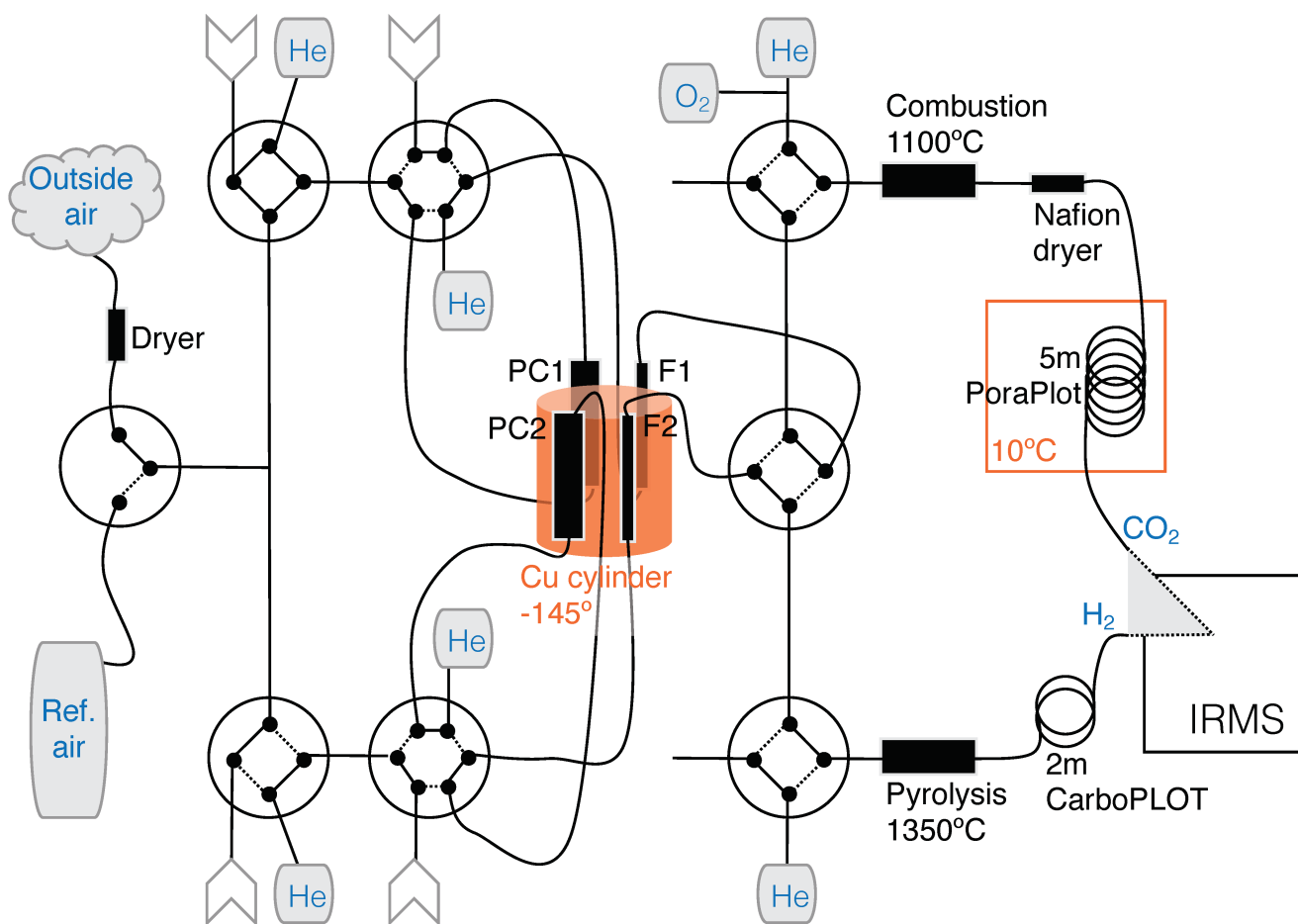
Figure S1: Diagram of the extraction system for methane isotopic measurements in ambient air. PC: pre-concentration, F: focus traps, two 10 cm stainless steal tubes (1/8" and 1/16" o.d., respectively) filled with 2 cm HayeSep D in the centre and glass beads at both ends.
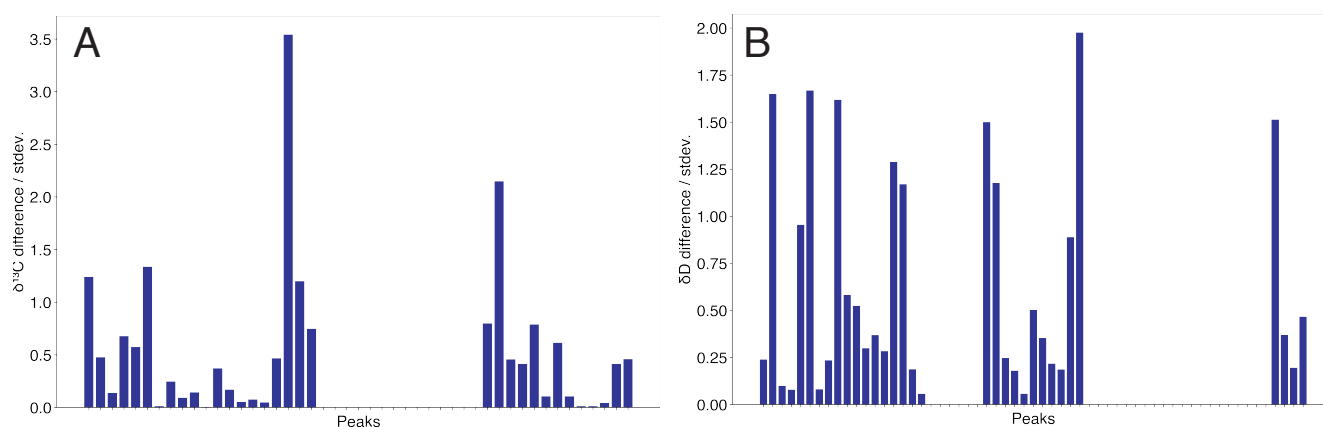
Figure S2: Ratio of the peak source signature difference between original and "corrected" $\chi(CH_4)$ data, over the original signature uncertainties (standard deviation, σ). For the "corrected" $\chi(CH_4)$, we applied an offset to the IRMS data to match the CRDS data in the periods where an offset was observed. Most differences are lower than 2σ for $\delta^{13}C$ (**A**), and δ^2H (**B**).
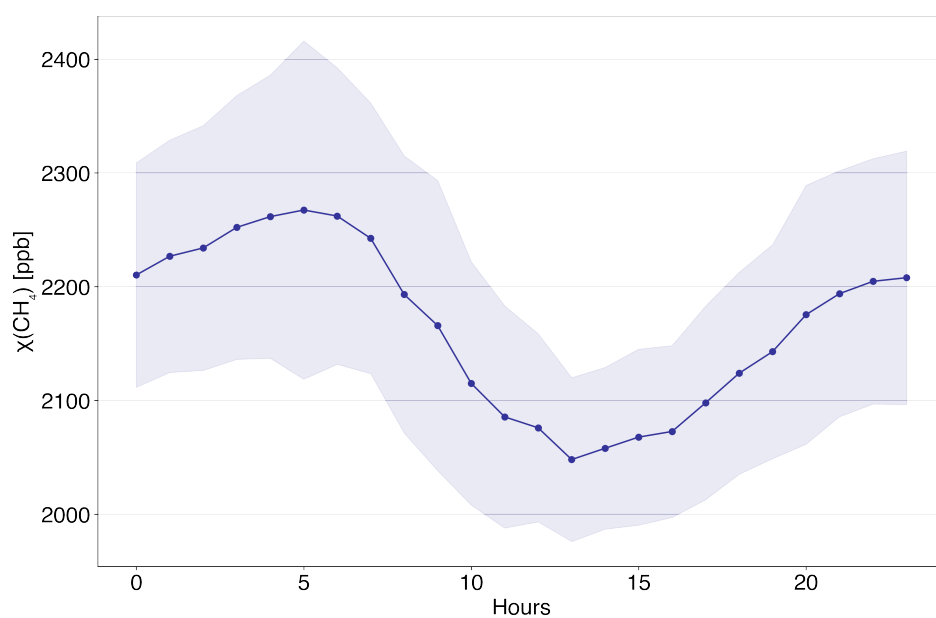
Figure S3: CH$_4$ mole fraction hourly averages during the fall (September 14 to November 15, 2018). Size of shaded area is 1σ.
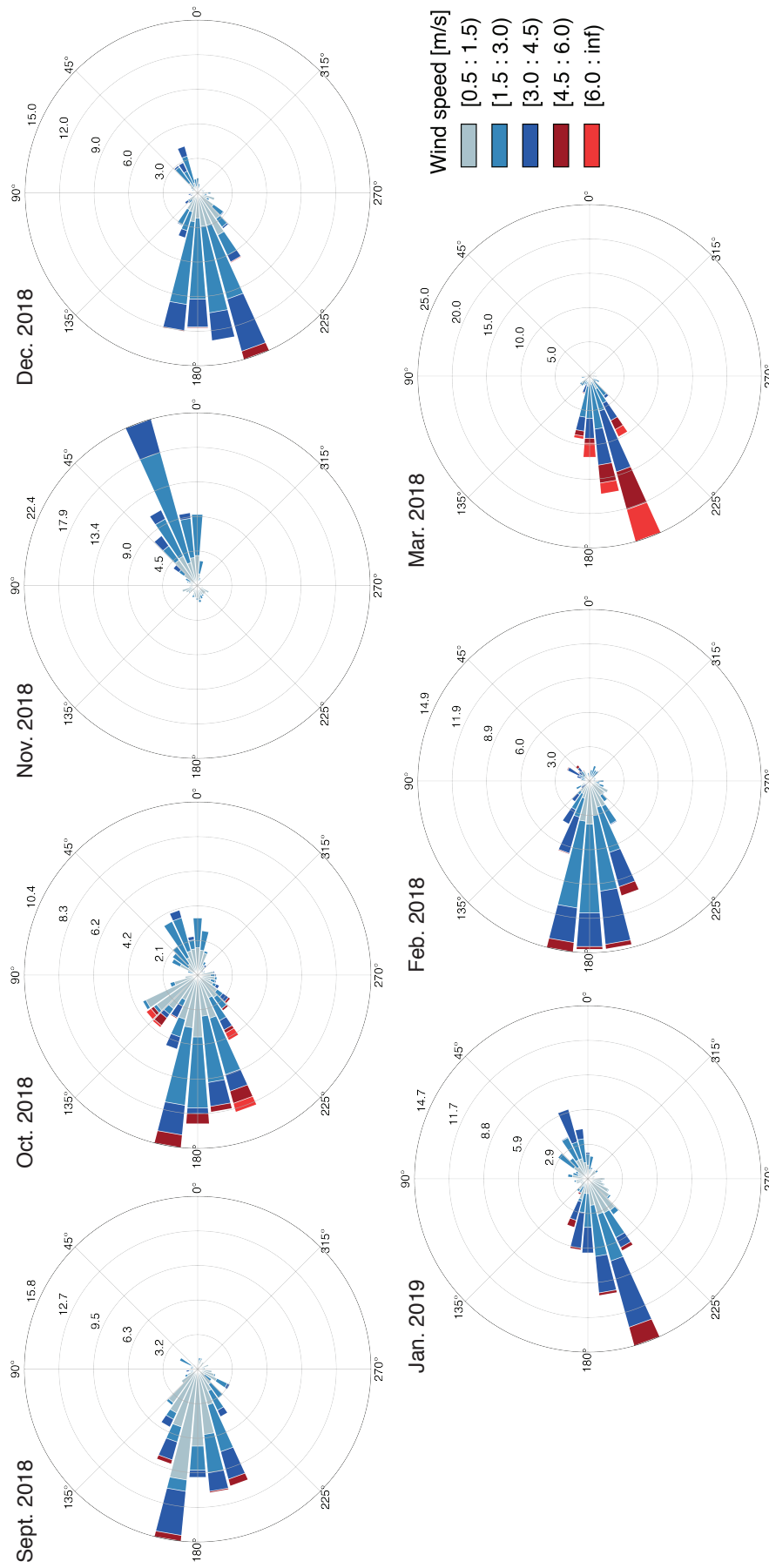
Figure S4: Monthly wind directions during the ambient air measurement period, at the measurement location. Bar lengths are percentages of record during the specified month (r-axis); colours define the wind speed range (legend).
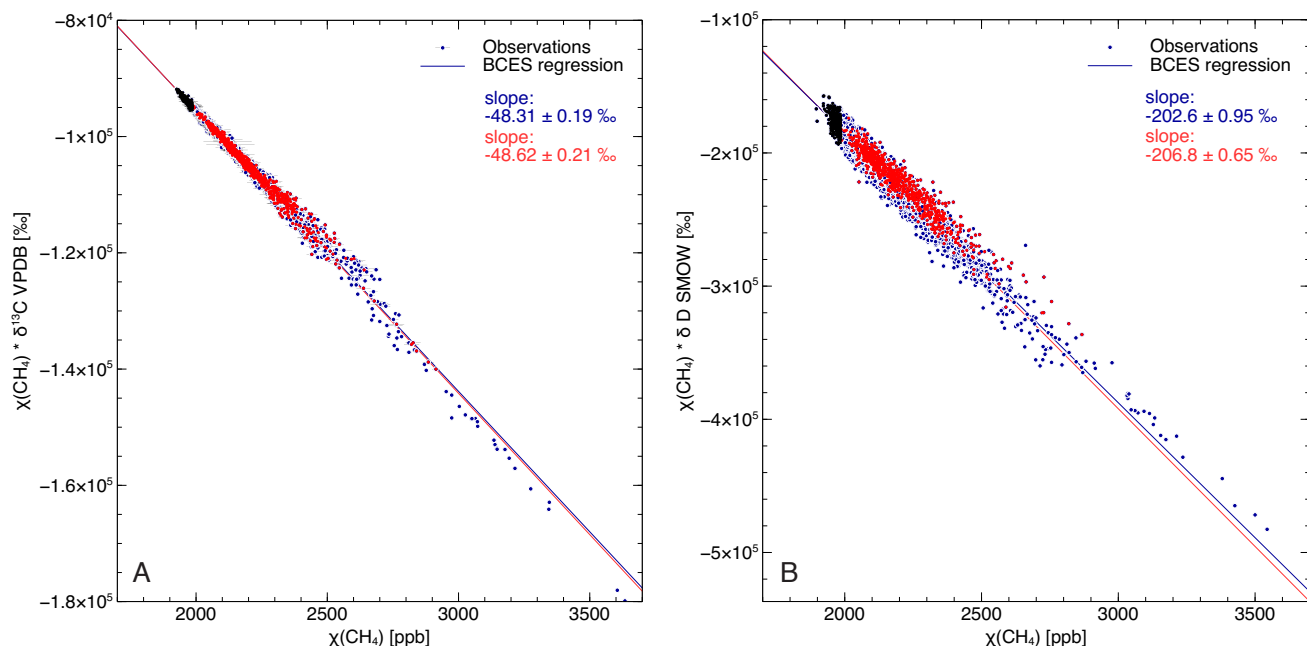
Figure S5: Miller-Tans plots using all the **A.** δ^{13}C-CH$_4$ and **B.** δ^2H-CH$_4$ data in ambient air collected during the measurement period. The red points show when there was a mismatch in the mole fractions between the IRMS and CRDS instruments, and the black points show the background data (χ(CH$_4$) < 1986.0 ppb, i.e. 10th lower percentile).
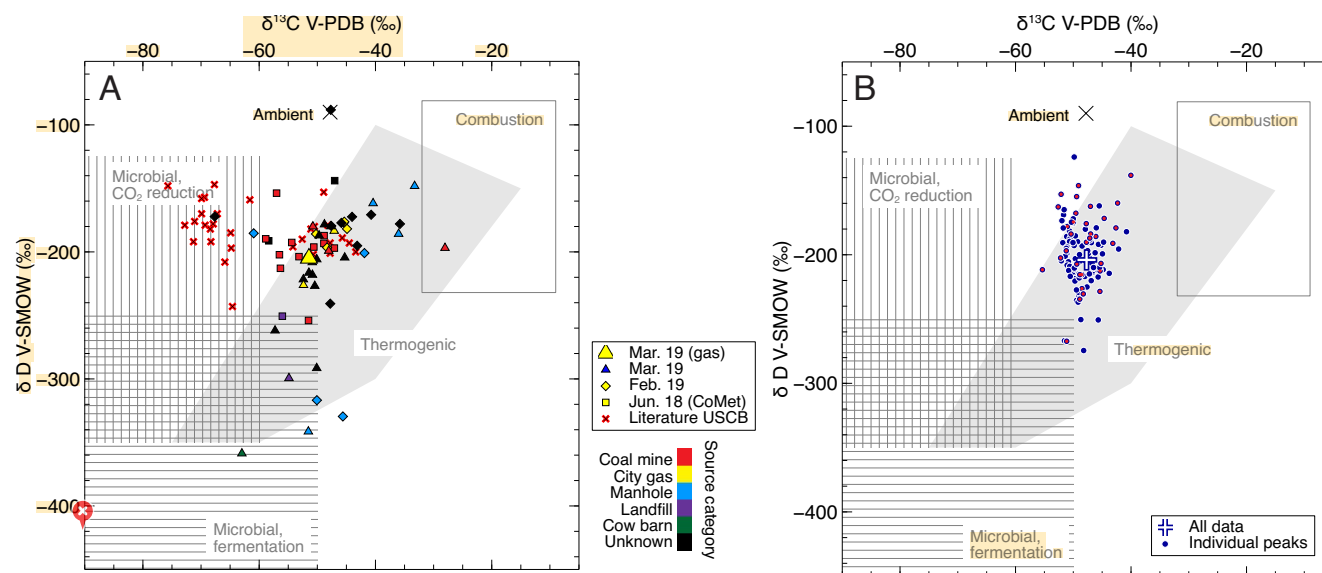
Figure S6: Dual isotope diagrams with signature ranges of specific CH$_4$ formation processes (background grey patterns), reproduced from Milkov and Etiope (2018). **A.** Source signatures of the sampled sites around Krakow and in the USCB (Kotarba 2001, Kotarba and Pluta 2009 and Kedzior et al. 2013). **B.** Source signatures of the emission peaks measured in ambient air. Red points: mismatch in the mole fractions between the IRMS and CRDS instruments, which peak isotopic signatures did not significantly differ (we retained all the data).
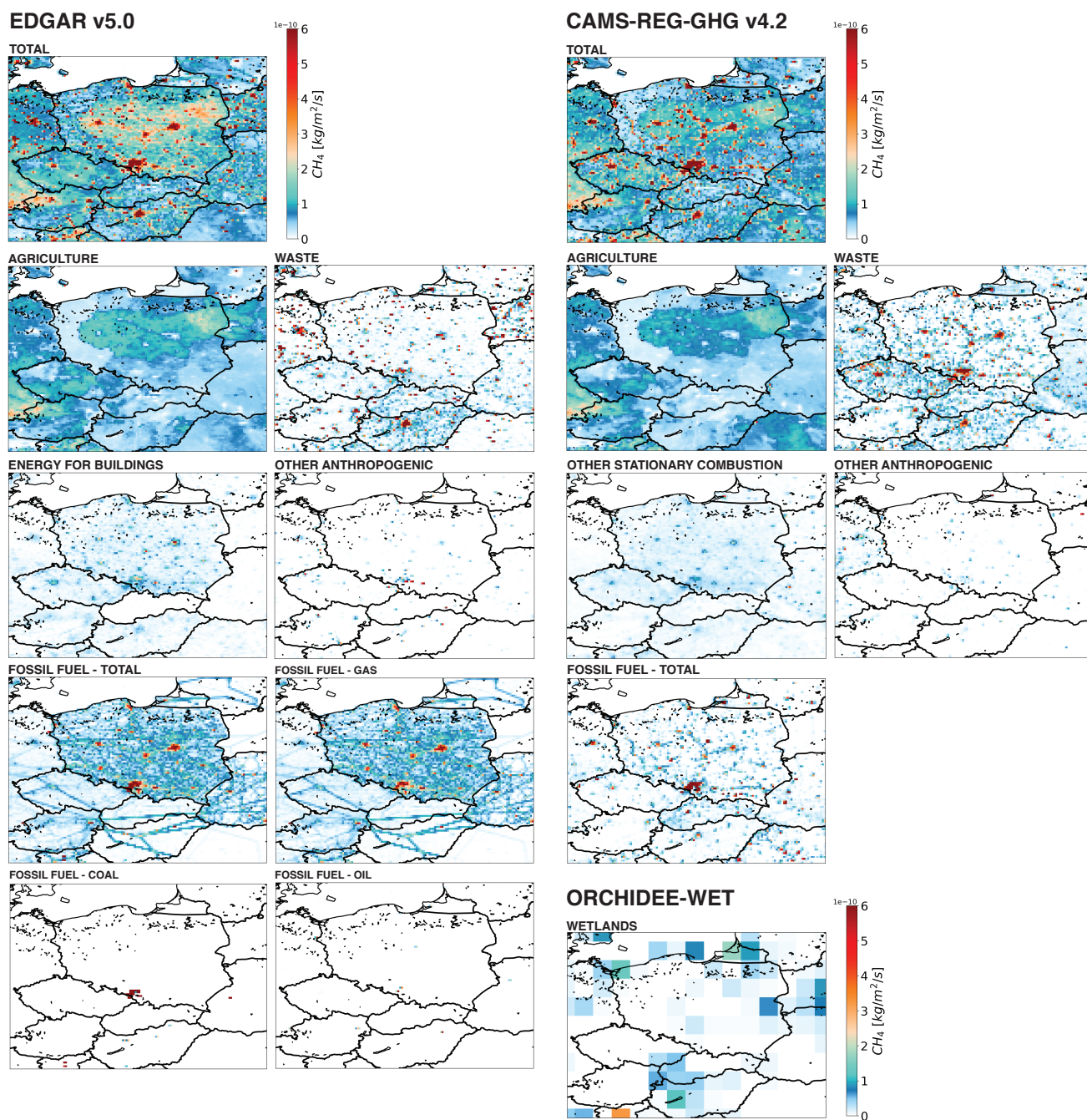
Figure S7: Reported CH$_4$ emission rates over the domain used in CHIMERE, from two inventories: EDGAR v5.0 (left columns) and CAMS-REG v4.2 (right column).